CIRCUIT AND ELECTROMAGNETIC SYSTEM DESIGN NOTES

Note 40

28 December 1990

Preliminary Considerations for High-Power Microwave (HPM) Radiating Systems

D. V. Giri
Pro-Tech, Suite No. 110
3708 Mt. Diablo Boulevard, Lafayette, CA 94549-3610

Abstract

The objective of this note is to discuss and study various aspects of an HPM radiating system. Several classical radiating systems are considered and their suitability for HPM application is considered. It is concluded that dual reflector antenna systems (e.g., an offset Cassegrain antenna) are well suited for efficiently broadcasting a directive HPM radiation. Future reports will consider a specific dual reflector antenna system in greater detail. Related topics such as power handling capacity of rectangular waveguides, near and far fields from an electromagnetic (EM) pyramidal horn and a review of HPM sources are also described in this note.

PREFACE

This work was performed by Pro-Tech for the Department of Electrical Engineering, University of California at Los Angeles (UCLA), and was sponsored by the U.S. Army. The author is thankful to Professor Y. Rahmat-Samii of UCLA for his encouragement and support. Dr. Carl Baum of Phillips Laboratory (AFSC) Kirtland AFB, NM assisted in compiling this note from a set of interim reports, initially submitted to UCLA.

CONTENTS

1. Introduction

In the context of generating directive HPM beams, the main goals of this study may be summarized as follows:

a) identify all of the critical antenna issues arising from the high power levels (1 to 10 GW peak),

b) study the feasibility of different antenna systems,

c) recommend a suitable design,

d) develop the mathematical models and computational tools required for synthesis and performance prediction,

e) carry out the antenna analysis leading to predicted performance including the radiated pulse characterization,

f) conceptual design of the experiments for low-level testing

g) recommendation for high-power testing

h) feasibility study of transportability of the antenna system.

In performing the above tasks, the technical guidelines we have followed are listed below:

a) pulse mode operation

b) 1 to 10 GW peak power

c) 200-800 ns pulse width

d) 1 to 3 GHz frequency of operation

e) flat-top radiated pulse

f) 30 to 40dB antenna gain

g) fixed mobile antennas with reasonable physical size

h) breakdown issues

i) 1 to 20 Hz pulse repetition frequency

j) moderate side lobe levels

k) beam scanning capabilities

A schematic of an antenna system for HPM is shown in figure 1-1. It consists of the HPM source from which the power is carried out in evacuated waveguides, followed by beam forming networks (ex: phase shifting or combining or splitting of waveguides etc.) that lead into a feed array, where the proper interfaces are placed to avoid breakdown. Finally, the radiating system broadcasts the HPM into far fields. This figure only shows the basic elements of the entire system.

In Section 2 of this paper, we consider several classical radiating systems and investigate their applicability for HPM radiation. We conclude in Section 2 that reflector antennas in general and an offset Cassegrain system in particular are well

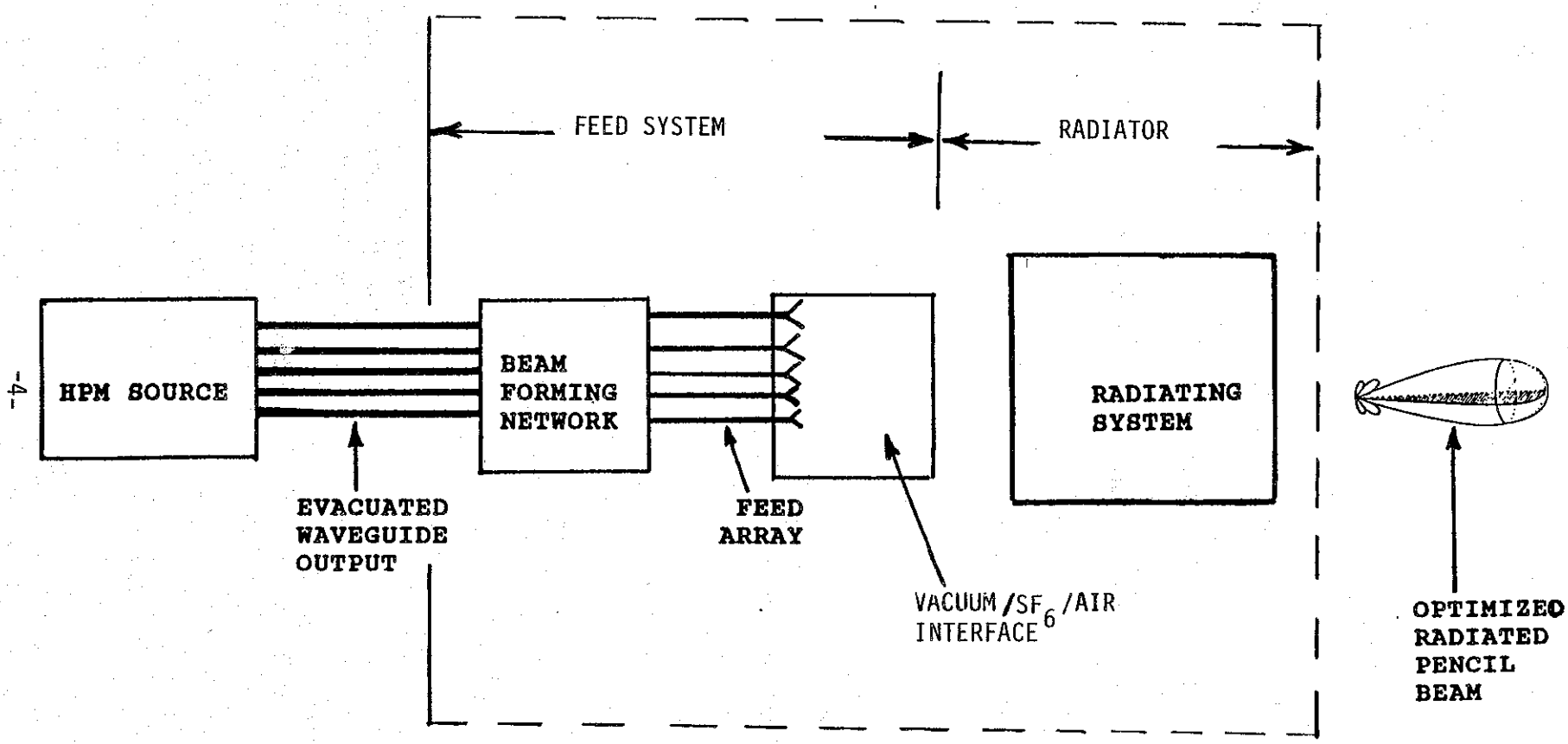

Figure 1-1. High-Power Microwave Antenna System Schematics.

suited for generating directive HPM beams.

Having chosen a dual reflector antenna system, one needs to develop the mathematical models and computational tools to synthesize the antenna system. Sections 3, 4, and 5 consider different aspects of the radiating system. In Section 6, we briefly review the status of HPM sources and the note is concluded by summarizing remarks in Section 7, followed by a list of references.

2. Radiating Systems for Producing Directive HPM Beams

We start with a basic assumption that the power from the HPM source is available from a number N ($\geq$ 1) of evacuated waveguides. A list of possible radiators are

a) leaky pipe or slots in waveguides
b) electromagnetic horn antenna
c) dielectric lens antenna
d) reflector antenna

All of the above antennas are classical in nature and are supported by well established theoretical and experimental characterization [1]. Using the above radiating elements, many types of radiating systems can be considered in meeting the present requirements [2]. They are shown in Table 1. The eight types of radiating systems listed in Table 1 are briefly considered below for their suitability in HPM application.

2.1. *An Array of Slotted Waveguides*

This system is basically an array of slots cut in the walls of an array of waveguides (rectangular for example). The slots can be resonant (i.e., slot spacing = $\lambda_g/2$) to produce a broadside beam or the slots can be non-resonant to produce a main lobe at some prescribed angle (θ, ϕ) where θ is the polar angle and ϕ is the azimuthal angle (figure 2-1). For HPM applications, the slots should have rounded edges to avoid excessive field enhancement, but the main problem appears to be the low value of the conductance of a slot which is typically in the range of 10^{-3} to 10^{-2} mhos per slot. Even assuming an electric field of about 1MV/m in the slot, the equivalent voltage across a slot of width = 2 cm (say) is about 20 kV. The average power radiated per slot

$$\begin{aligned} P_{slot} &\simeq \frac{1}{2} V^2 G_{slot} \\ &\simeq \frac{1}{2} (2\times10^4)^2 \times 10^{-2} \simeq 2MW \end{aligned} \tag{2.1}$$

This suggests, one requires hundreds or even thousands of slots to radiate several GW of HPM. Such antenna systems are suited in flush-mounted aerodynamic applications and can be ruled out in the present context.

2.2. *Horn Array*

Figure 2-2 shows a circular aperture formed by an array of horns. The fields in each horn can be uniform in phase and amplitude. The disadvantages of such an array or any other array (rectangular array) of horns is that it takes too many horns to come up with a large aperture plane in terms of wavelength dimensions. In addition, there are vertical lines where pairs of horns are joined, that have zero electric field, resulting

Basic Radiator		The Radiating System
1) Slots in waveguide	→	An array of slotted rectangular waveguides
2) EM horn antenna	→	An array of horns
3) Dielectric lens antenna	→	Single large dielectric lens Dielectric lens array
4) Reflector antenna	→	Large dish An array of dishes Cassegrain reflector (dual reflector system) Offset Cassegrain system

Table 1. Eight possible radiating systems from the four basic radiating elements.

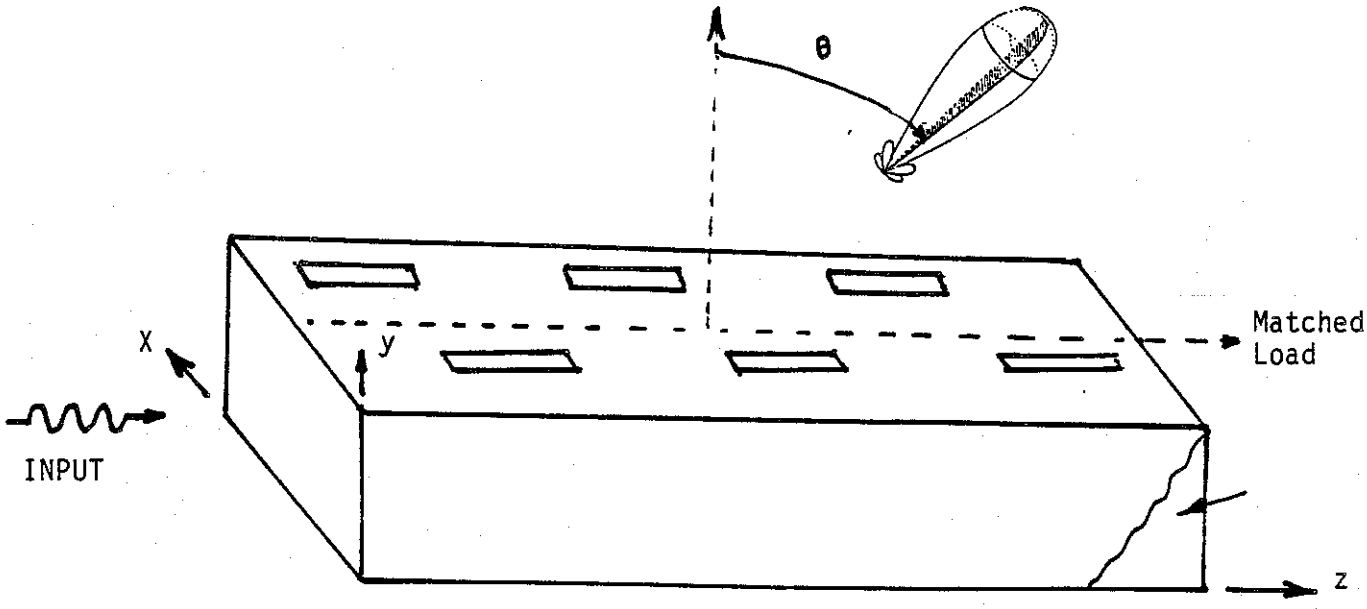

Figure 2-1. Slotted waveguide system consisting of nonresonant.

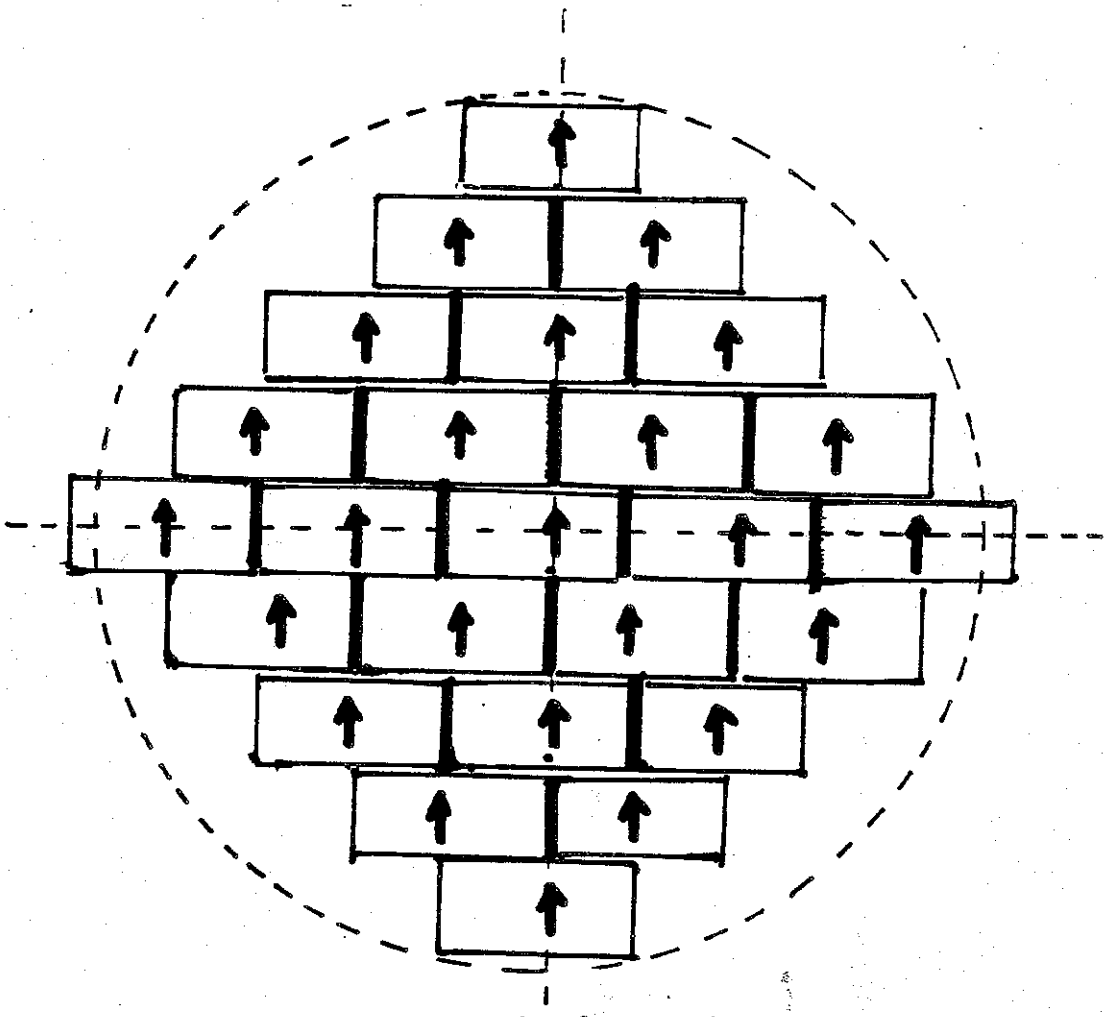

Figure 2-2. Horn array that fills a circular aperture.

in "cold spots" in the aperture plane which are not desirable.

In general, larger the radiating aperture, smaller will be the beam in the far field. The angular width of the main lobe is inversely proportional to aperture dimensions measured in wavelengths. The circular aperture has the added benefit of equal angular widths of the beam in both planes.

2.3 *A Large Dielectric Lens Antenna*

A large dielectric lens of figure 2-3 can be built to radiate a narrow beam in the far field. The equation for surface S_1 is easily found by requiring that the portion of the aperture plane S_2 be a wavefront. This results in [1],

$$r + nd = f + nd_0 \tag{2.2}$$

where the symbols r, d, f and d_0 are defined in figure 2-3 and n is the refractive index of the lens. Also the distance d is given from geometrical conditions

$$d = f + d_0 - r\cos\theta \tag{2.3}$$

we then have

$$r = \frac{(n-1)f}{n\cos\theta - 1} \tag{2.4}$$

which is an equation of a hyperbola for the surface S_1. Once again the problem here will be to obtain a large aperture (several tens of wavelengths in size). The fabrication of a large dielectric lens is somewhat impractical.

2.4. *Dielectric Lens Array*

An array of dielectric lenses, in which each lens is fed by its own horn is shown in figure 2-4. Once again, the object is to make the exit rays uniform in amplitude and phase in order to produce a narrow beam in the far field. This method requires a large number of lenses and horns and could have "cold spots" in the aperture plane. Such cold spots result in an inefficient use of the aperture surface. The electromagnetic fields from aperture antennas can be represented as integrals over the aperture field. Baum [3] has considered the problem of maximizing the fields at an observer with focused apertures.

2.5. *Large Dish Antenna*

Figure 2-5 schematically shows a large (in terms of wavelengths) antenna that can be fed by a single horn at the focal point or a cluster feed arrangement, if power from the source is carried by many waveguides. This is an efficient way of broadcasting HPM, especially if no beam steering is required. In this case beam-steering is achieved by rotating the large dish which can be impractical in certain applications.

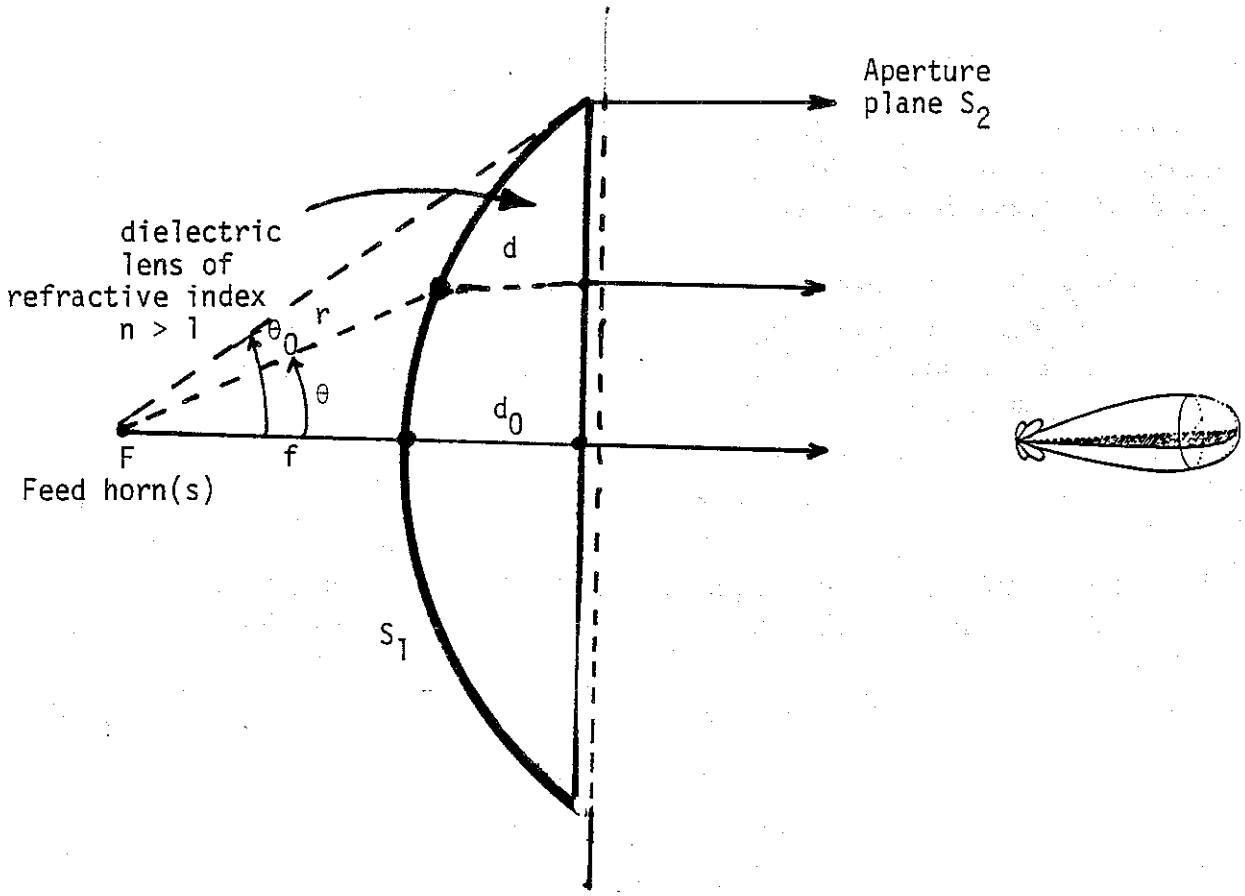

Figure 2-3. A large single dielectric lens antenna.

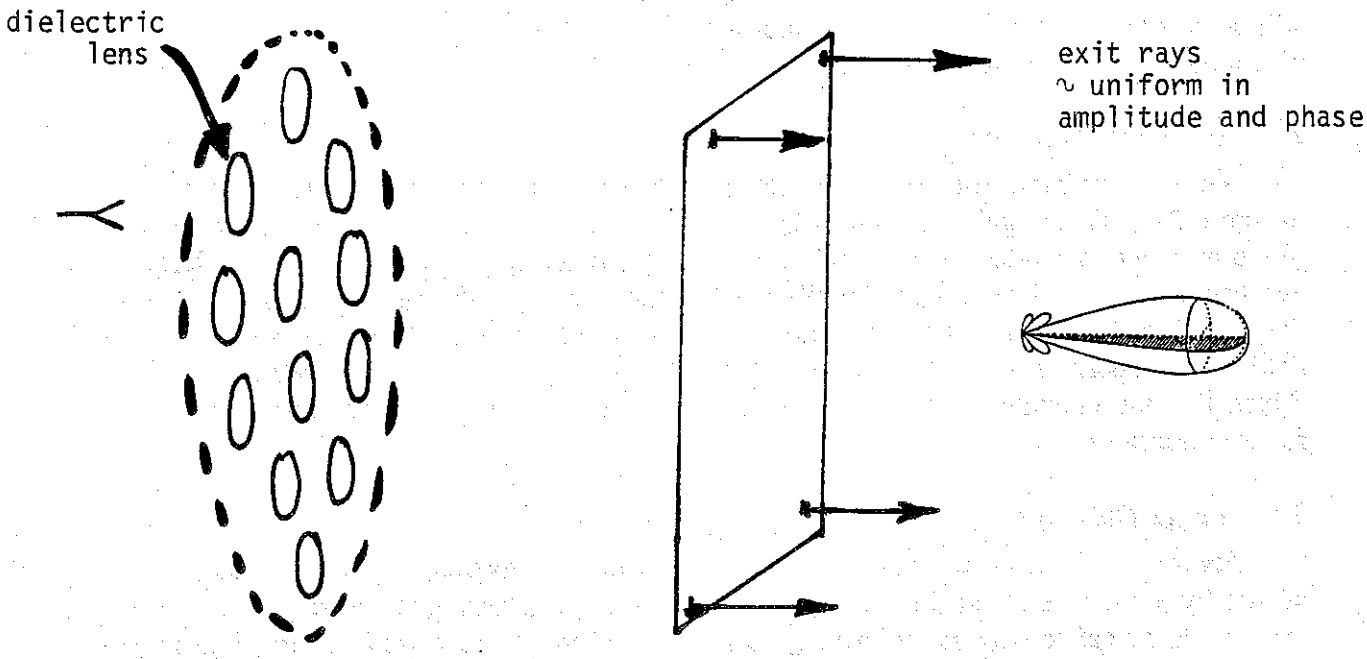

Figure 2-4. Dielectric lens arrays.

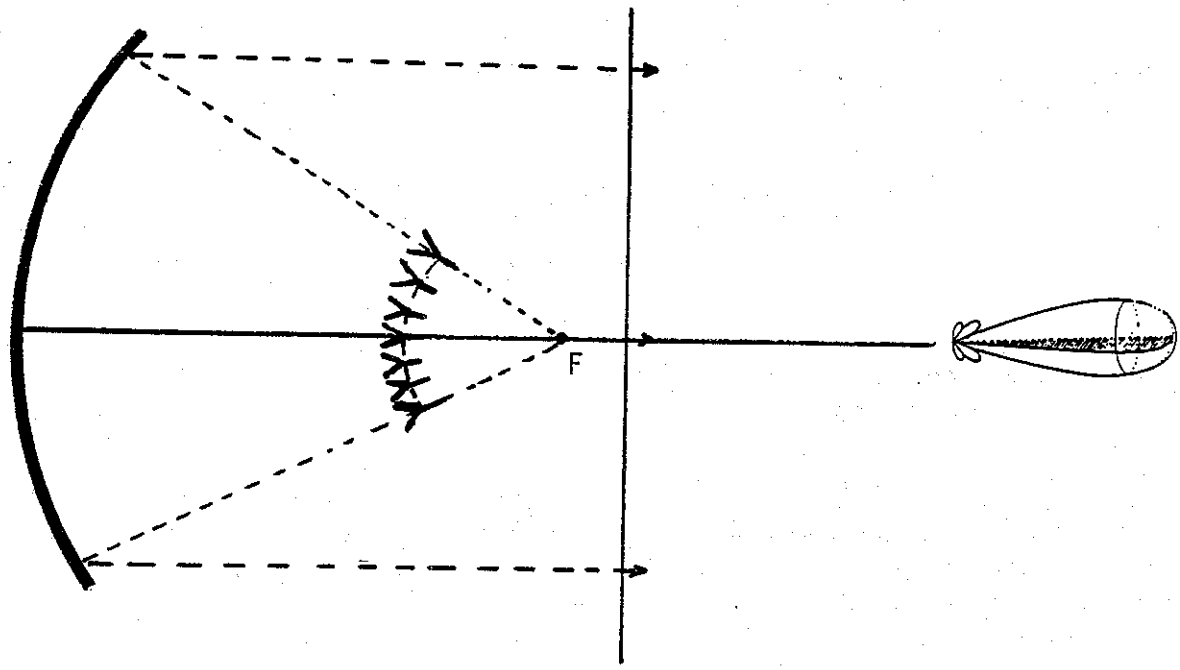

Figure 2-5. A large dish antenna which is cluster fed by a set of horns on a spherical surface.

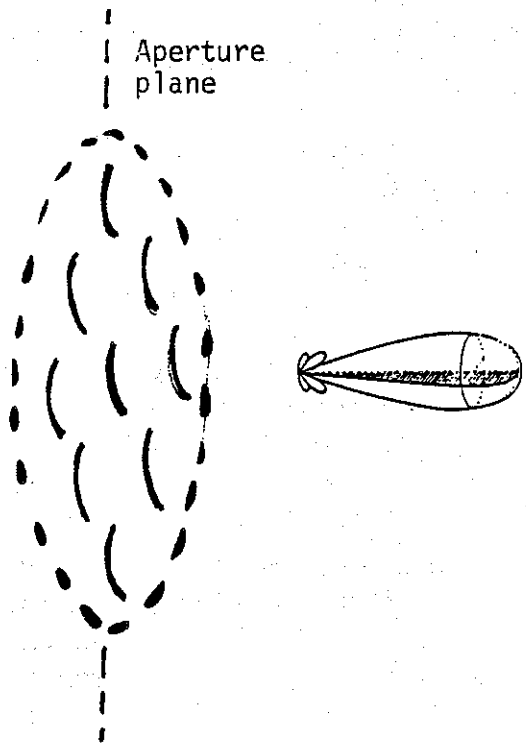

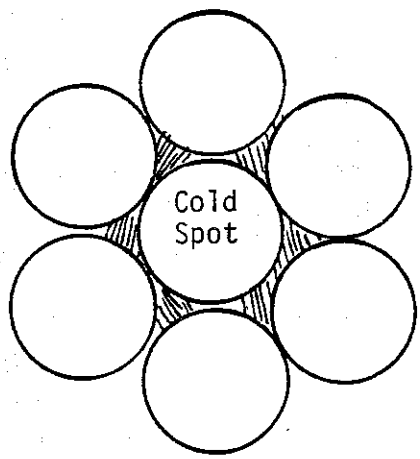

front view of a hexagonal (approximating a circle) array of dishes

Figure 2-6. An array of offset fed dish antennas.

2.6. *An Array of Dish Antennas*

An array of dish antennas in which each dish is offset-fed by a single horn is shown in figure 2-6. As in the case of an array of dielectric lenses, one requires a large number of dishes, horns and the radiating aperture will still have "cold spots" or regions of zero fields, which are undesirable in producing a narrow beam in the far field.

We also observe that when one has many feed elements to drive, two schemes of excitation are possible in theory as indicated in figures 2-7 and 2-8. In figure 2-7, one oscillator drives several feed elements and in figure 2-8, we have several phase-locked oscillators employed to drive the different feed elements. Phase locking of HPM sources is being investigated by other researchers [4]. They indicate that extending the power levels well beyond 10 GW groups of oscillators are a likely approach, in which case phase locking becomes essential.

2.7. *Cassegrain System*

This is a dual reflector antenna shown in figure 2-9 where the smaller subreflector is a hyperbolidal surface and the larger main reflector is a paraboloid. This is an efficient way to broadcast a narrow beam in the far zone, but the disadvantages are: a) beam steering is relatively more difficult compared to the offset Cassegrain system and b) the aperture blockage.

2.8. *Offset Cassegrain System*

The aperture blockage in figure 2-9 is avoided in figure 2-10 by offsetting the dual reflector [5]. Beam steering is also feasible to a limited extent by keeping the main paraboloidal reflector fixed and moving the smaller hyperboloidal subreflector.

We have thus far considered eight different antenna systems and their essential features, for HPM application are listed in Table 2. This table lists hardware requirements, performance and problems, and a ranking of the various systems. The comparisons of various antenna system in Table 2, leads us to recommend the use of an offset Cassegrain system fed by one or more pyramidal horns. Some amount of steering is possible by moving the subreflector. At lower power levels, electronic steering has been successfully employed [6]. The electronic steering in general consists of: target sensing, computing propagation delays (equivalently phase shifting) for individual elements and adjusting for these delays by computer controlled delay circuits. This method is impractical at high power levels, where phase shifting or delay lines technology for evacuated waveguide runs is yet to be developed. For the present, mechanical steering by moving a small sub reflector is the option, we are investigating.

In addition to the eight different antenna systems considered above, one may wish to consider a cylindrical monopole above a ground plane and a log-periodic antenna. However both of these radiating systems are unsuitable in the HPM context. The base driven monopole has a null in the axial direction and it is impractical to deliver high power levels from the source to a pair of terminals as required by both the dipole and the log-periodic antennas.

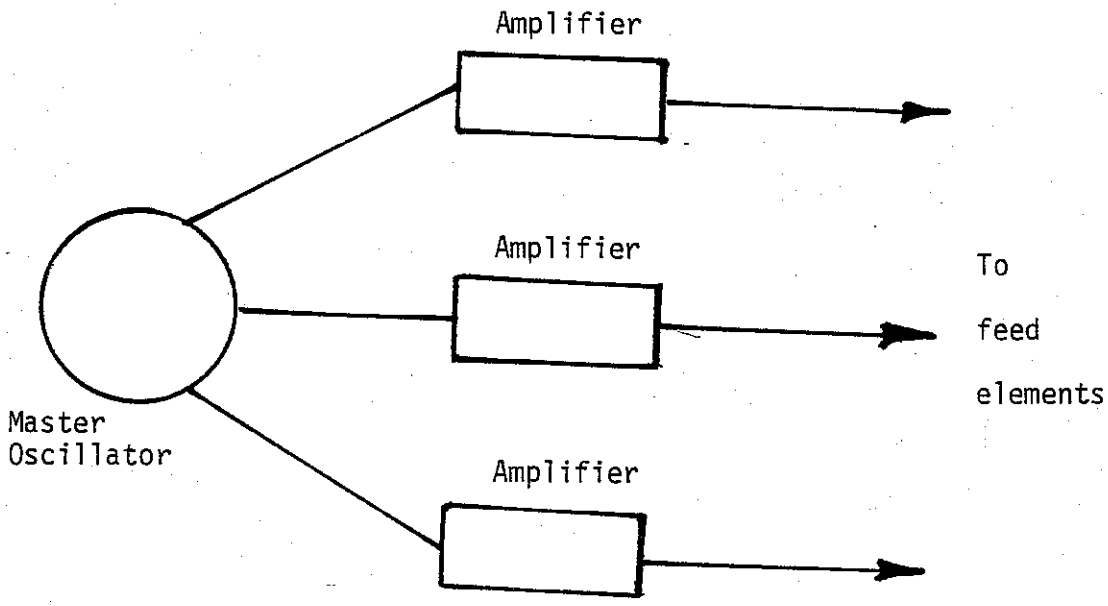

Figure 2-7. A single source driving several feed elements.

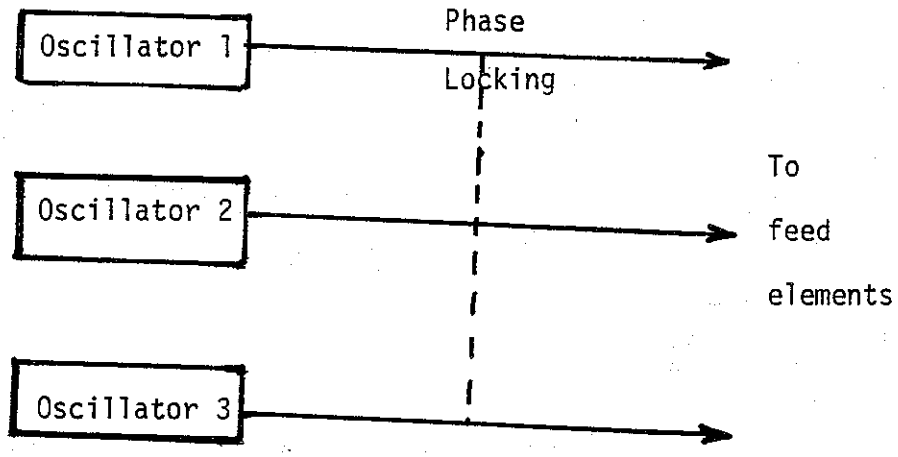

Figure 2-8. Several phase-locked sources driving several feed elements.

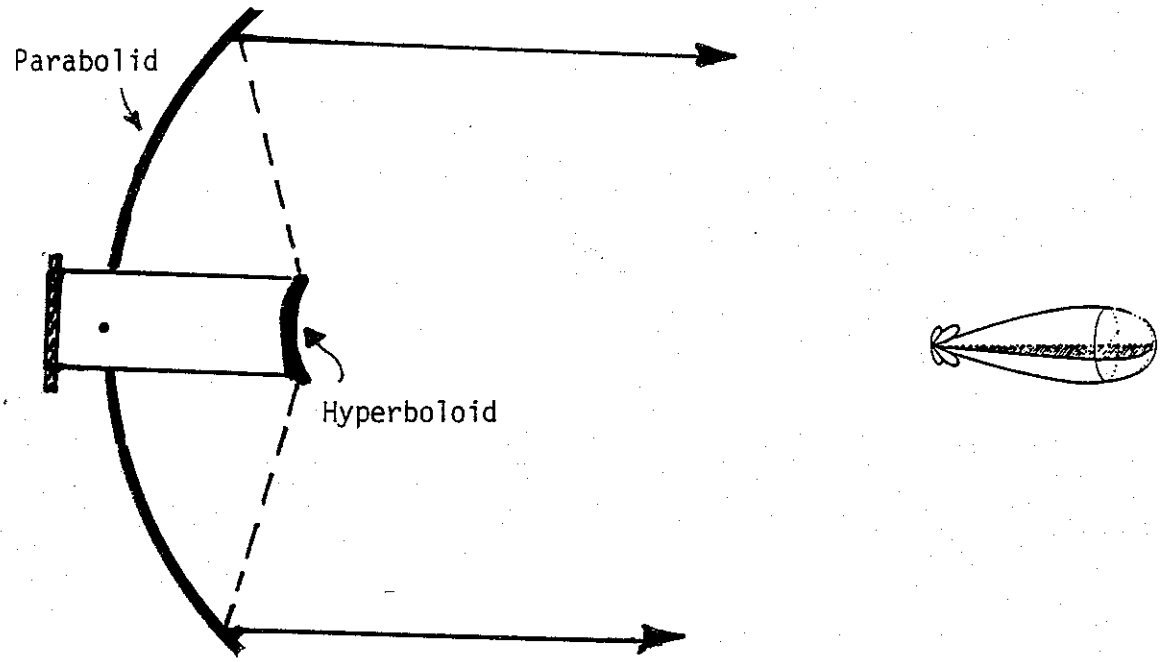

Figure 2-9. Cassegrain system.

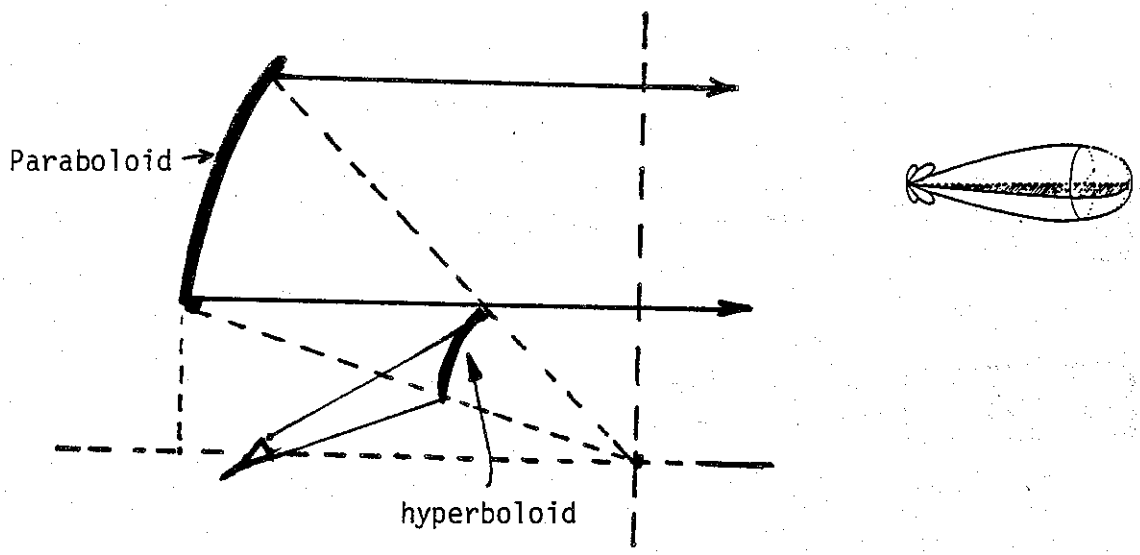

Figure 2-10. Offset Cassegrain system.

Name		Horn Array Figure 3	Dielectric Lens Array Figure 5	Dish array Figure 7	Large dielec lens: Figure 4	Large dish Figure 6	Cassegrain Figure 10	Leaky pipe Figure 2	Offset Cassegrain Figure 11
Hardware	Feed Lines	Rectangular WG lines evacuated/SF_6 at 1 at m/SF_6 pressurized							
	Phase Shifters	High Power level Phase Shifters required							
	Interface	Global (= 1)	individual (= # of horns)	individual	Global	Global	Global	One	Global
	Horns	$\frac{\pi r^2}{A_H} = \frac{\pi \times 1.5^2}{.25^2}$ ~ 100	5 to 10	5 to 10	5 to 10	5 to 10	$\sim$ 10	None needs develop. of matched load	$\sim$ 10
Performance & Problems		•Single horn well known •Array factor well known •easy to calc.	•lens design well known •some cold spots •construction relatively harder	•dish design well known •some cold spots	•lens is large (2 to 3 m) •mfg. difficult •cluster feed	•simplest •cluster feed	•cold in the middle •need to offset	•Rule out for HPM	•Avoids Aperture blockage
Ranking for Target Illumination in far field		5	6	4	7	2	3	Ruled out	1

TABLE 2. Ranking of the various concepts for Directing HPM Radiation at targets in the far field

2.9. *An Illustrative Example of an Offset Cassegrain*

The offset Cassegrain system is considered here for illustration. The geometry and design equations are indicated in figure 2-11, and an example is presented in figure 2-12. The 10 dB beam width is about 1 degree in both planes and about 20 beam widths i.e., 20° steering in both θ and ϕ should be possible by moving the feed. The offset Cassegrain system of figure 2-11 uses a single feed horn. A cluster feed would require placing several horns with their apertures on an approximately spherical surface. The horn arrangement on a spherical surface will be considered in a future memo.

With regards to the electric field produced at a distance, one may *estimate* this in the far zone by using

$$\frac{E_{far}}{E_0} \simeq \frac{A}{R\,\lambda} \tag{2.5}$$

where

E_{far} = far electric field at the target
E_0 = field at the antenna aperture
A = aperture area
R = distance to target
λ = wavelength

Writing (2.5) in terms of power densities we have

$$\frac{S_{far}}{(P_{tot} \times \eta / A)} = \frac{A^2}{R^2 \lambda^2} \tag{2.6}$$

where

S_{far} = Power density at the target (W/m^2)
P_{tot} = total power from the HPM source (Watts) = $P_{dc}\ \eta_{source}$
η = efficiency of power transfer from source to the radiating aperture*
P_{dc} = dc power supplied to the HPM source

Equation (2.6) leads to

---

*Note that η indicates a power transfer efficiency from the output of the HPM source ot the radiating aperture. It does not include the efficiency of the HPM source itself η_{source}, which is typically below 35%.

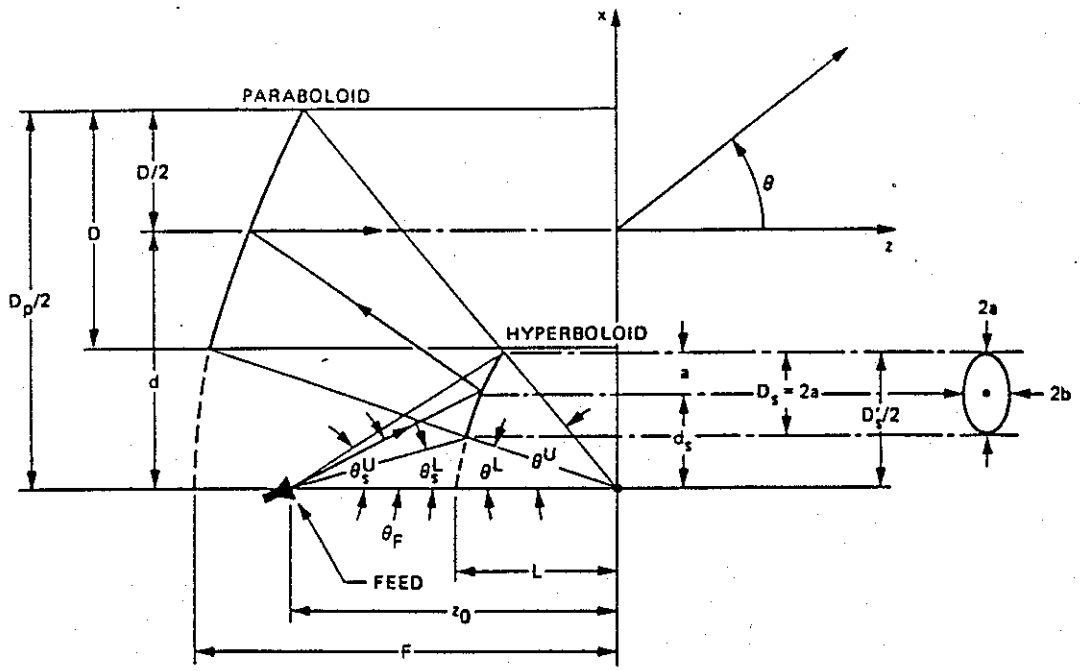

Paraboloid main reflector:

$$\theta^B = \frac{\theta^U + \theta^L}{2} \tag{1}$$

$$\theta^C = \frac{\theta^U - \theta^L}{2} \tag{2}$$

$$D = \frac{4 \sin \theta^C}{\cos \theta^B + \cos \theta^C} F \tag{3}$$

$$d = \frac{2 \sin \theta^B}{\cos \theta^B + \cos \theta^C} F \tag{4}$$

$$\theta_{U,L} = 2 \tan^{-1} \frac{d \pm D/2}{2F}. \tag{5}$$

Hyperboloid subreflector:

$$M = \frac{\tan \theta^U/2}{\tan \theta_s^U/2} = \frac{\tan \theta^L/2}{\tan \theta_s^L/2} = \frac{\tan \theta/2}{\tan \theta_s/2} \tag{6}$$

$$e = \frac{M+1}{M-1} \tag{7}$$

$$\theta_s^B = \frac{\theta_s^U + \theta_s^L}{2} \tag{8}$$

$$\theta_s^C = \frac{\theta_s^U - \theta_s^L}{2} \tag{9}$$

$$\frac{Z_0}{L} = 1 + M \tag{10}$$

$$d_s = \frac{(1+e)(e \cos \theta^B + \cos \theta^C) \sin \theta^B}{(1-e^2) \sin^2 \theta^B + (\cos \theta^B + e \cos \theta^C)^2} L \tag{11}$$

$$\frac{Z_0}{D_s'/2} = \frac{1}{\tan \theta^U} + \frac{1}{\tan \theta_s^U} \tag{12}$$

$$\frac{Z_0}{D_s'/2 - 2a} = \frac{1}{\tan \theta^L} + \frac{1}{\tan \theta_s^L} \tag{13}$$

$$a^2 = \frac{(1+e)^2 (\cos \theta^B + e \cos \theta^C)^2 \sin^2 \theta^C}{[(1-e^2) \sin^2 \theta^B + (\cos \theta^B + e \cos \theta^C)^2]^2} L^2 \tag{14}$$

$$b^2 = \frac{(1+e)^2 \sin^2 \theta^C}{(1-e^2) \sin^2 \theta^B + (\cos \theta^B + e \cos \theta^C)^2} L^2 \tag{15}$$

Figure 2-11. An offset Cassegrain system with the design equations from Reference [5].

Example Parameters [Ref. 5] (see figure 12)

$D = 100\ \lambda = 30$ m
$d = 70\ \lambda = 21$ m
$F = 96\ \lambda = 28.8$ m
$z_0 = 25\ \lambda = 7.5$ m

for an example $\lambda = 0.3$ m
or $f = 1$ GHz

$\theta^B = 37.95°$

$\theta^C = 26.06°$

$M = 1.5$

$\theta_s^B = 26.59°$

$\theta_F = 27.32°$

case 1) $a = 7.4\ \lambda$; $b = 6.08\ \lambda$ (optical limit subreflector)

case 2) $a = 7.4\ \lambda$; $b = 7.08\ \lambda$ (subreflector extended by $1\ \lambda$)*

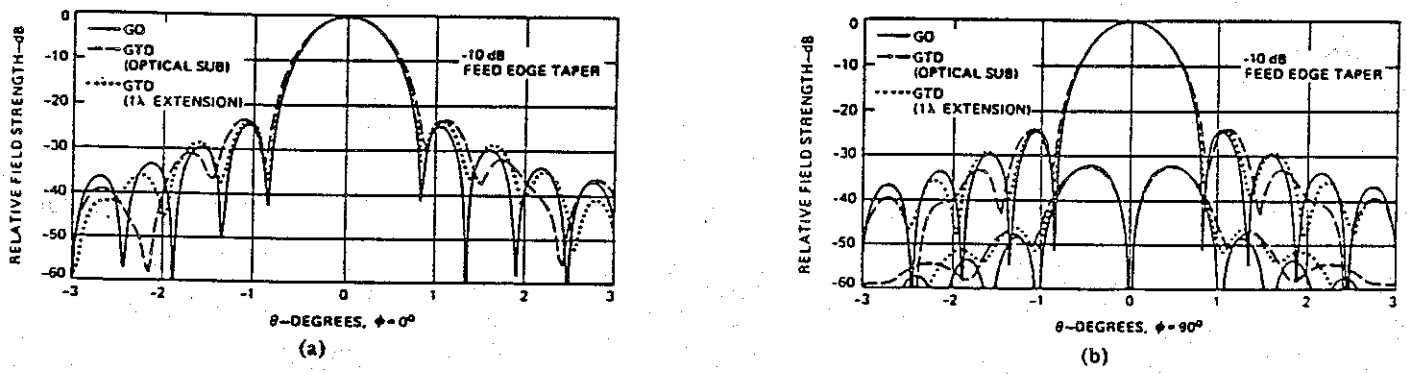

(x-z) plane (y-z) plane

Figure 2-12. Far field pattern of the offset Cassegrain reflector antenna shown in figure 2.

*The aperture's over all efficiency is improved by the $1\ \lambda$ extension on the reflector.

$$A = \frac{S_{far} R^2 \lambda^2}{P_{tot} \times \eta} \tag{2.7}$$

Some sample calculations of radiating aperture areas are shown in Table 3.

We have considered a brief review of classical radiators for their applicability and suitability in broadcasting HPM radiation. Possible radiators are slotted waveguides, electromagnetic horns, dielectric lenses and reflector antennas in the frequency range of interest (1 to 3 GHz). Several antenna systems were considered that make use of these basic radiators. A comparison of their performance characteristics has led us to recommend reflector antennas as an efficient way to produce a narrow beam in the far field. Among the reflector antennas, an offset Cassegrain system can be designed to meet the HPM radiation requirements, along with a limited (about 20 beam widths or 20° in both θ and ϕ direction) steering capability. Extensive future studies are required to address all aspects of such a radiating system such as a) survey of HPM sources b) power handling capacity of waveguides, c) breakdown issues and d) single horn and multi horn feed systems, etc. Some of these topics are considered in the following sections.

Case 1

f = 1 GHZ
S_{far} = 100 W/m^2
R = 50 km
λ = 0.3 m
$E_{far} \simeq 195$ V/m = $\sqrt{Z_0 S_{far}}$
P_{tot} = 1 GW
η = 0.75
=> A = 30 m^2
6.2 m dia. dish
dia = 20 wavelengths

Case 2

f = 3 GHz
S_{far} = 100 W/m^2
R = 50 km
λ = 0.1 m
$E_{far} \simeq 195$ V/m
P_{tot} = 1 GW
η = 0.75
=> A = 3.33 m^2
2 m dia dish
dia = 20 wavelengths

Case 3

f = 1 GHZ
S_{far} = 100 W/m^2
R = 100 km
λ = 0.3 m
$E_{far} \simeq 195$ V/m = $\sqrt{Z_0 S_{far}}$
P_{tot} = 1 GW
η = 0.75
=> A = 120 m^2
12.4 m dia. dish
dia = 41 wavelengths

Case 4

f = 3 GHz
S_{far} = 100 W/m^2
R = 100 km
λ = 0.1 m
$E_{far} \simeq 195$ V/m
P_{tot} = 1 GW
η = 0.75
=> A = 13.33 m^2
4.1 m dia dish
dia = 41 wavelengths

TABLE 3. Sample calculations of radiating aperture areas.

3. Power Handling Capacity of Rectangular Waveguides

Rectangular waveguides have been routinely employed in propagating microwave radiation in many applications. In the context of HPM, however, the power handling capability becomes important. We assume that the HPM radiation has a Gaussian envelop for the power and the microwave source, shown in figure 3-1 can be modeled by

$$P_m(t) = P\, e^{-[\alpha(t-\tau)^2]} \quad \text{(Watts)} \tag{3.1}$$

where P is the peak power occurring at $t = \tau$. In the terminology of the distribution of a random variable [7], the above equation represents the envelop of the output power and has a mean value of τ and a standard deviation σ related to the exponent α via

$$\sigma^2 = \frac{1}{2\alpha} \quad \text{or} \quad \alpha = \frac{1}{2\sigma^2} \tag{3.2}$$

Embedded in the envelop of the output power is the sinusoidal HPM signal as indicated in figure 3-2. It is the transmission of this sinusoidal EM wave in the rectangular waveguide that we are concerned about. T is the period of the HPM signal and is the reciprocal of the HPM source frequency f. For an assumed f of 1 GHz and 3 GHz, the corresponding values of T are 1 ns and 333 ps. So, thee are tens of even hundreds of periods of HPM in a single standard deviation of the output power envelop. The output power from the source, sketched in figure 1 may last for 200 - 800 ns. For harmonic time dependence of $e^{j\omega t}$, the instantaneous electric and magnetic fields in the waveguide are

$$\vec{E}(\vec{e},t) = \text{Real}\,[\tilde{\vec{E}}(\vec{r},\omega)\, e^{j\omega t}] \tag{3.3}$$

$$\vec{H}(\vec{r},t) = \text{Real}\,[\tilde{\vec{H}}(\vec{r},\omega\, e^{j\omega t}] \tag{3.4}$$

and the Poynting vector is given by

$$\tilde{\vec{P}}(\vec{r},\omega) = \frac{1}{2}\,\text{Real}\,[\tilde{\vec{E}},\omega) \times \tilde{\vec{H}}^{*}(\vec{r},\omega)] \tag{3.5}$$

where the * indicates complex conjugation and the position vector $\vec{r}$ denotes the location in the waveguide. Of course $\tilde{\vec{E}}$ and $\tilde{\vec{H}}$ satisfy Maxwell's curl equation according as

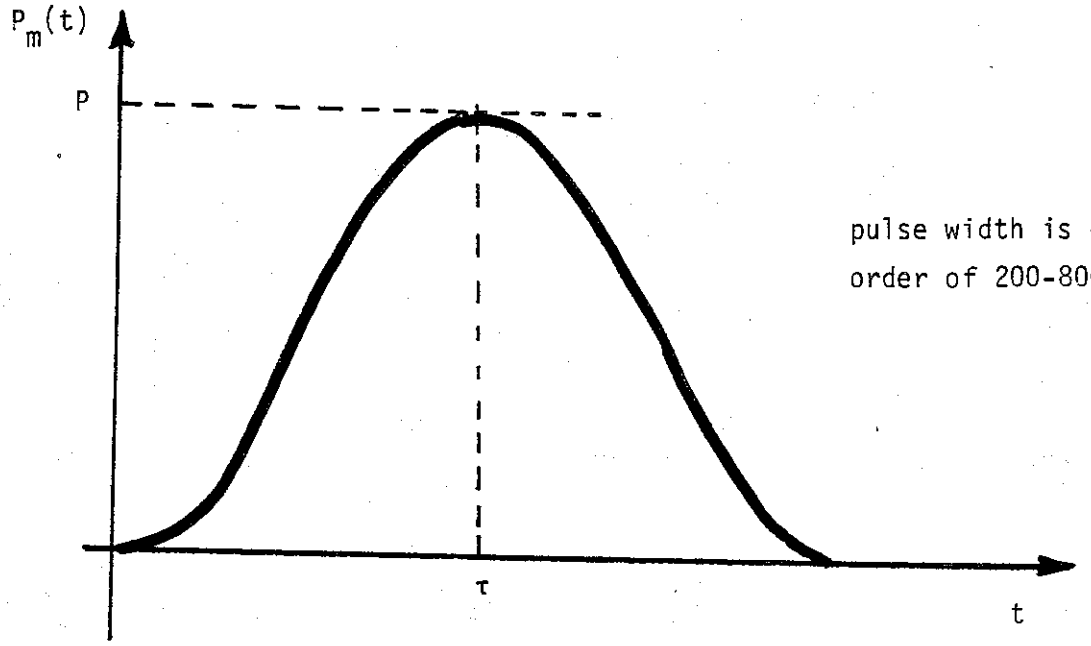

Figure 3-1. Typical output power from a HPM source , $P_m(t) = P \exp[-\alpha(t-\tau)^2]$

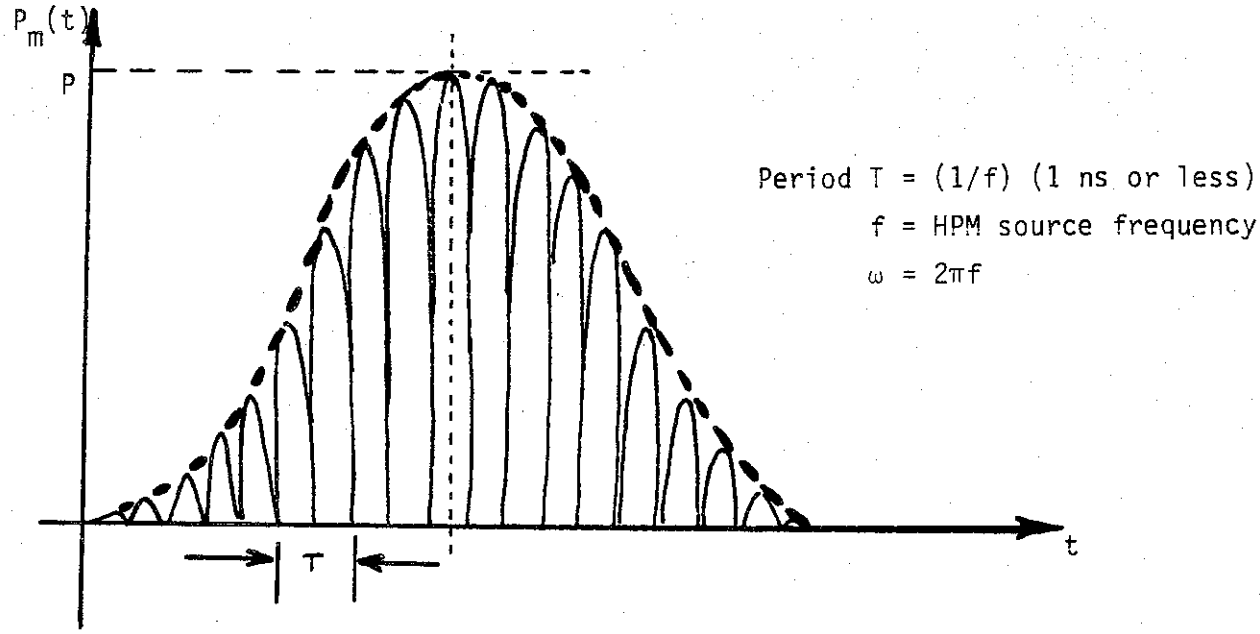

Figure 3-2. Same as above with the sinusoidal HPM signal embedded in it

$$\nabla \times \tilde{\vec{E}} = -j\omega\mu_0 \vec{H} \quad ; \quad \nabla \times \tilde{\vec{E}}^* = j\omega\mu_0 \tilde{\vec{H}}^*$$
$$\nabla \times \tilde{\vec{H}} = \tilde{\vec{J}} + j\omega\varepsilon_0 \tilde{\vec{E}} \quad ; \quad \nabla \times \tilde{\vec{H}}^* = \tilde{\vec{J}}^* - j\omega\varepsilon_0 \tilde{\vec{E}}^* \tag{3.6}$$

for an evacuated waveguide in which $\mu = \mu_0$ and $\varepsilon = \varepsilon_0$.

Having established the notation for HPM signals and output power, we proceed to review the fields in a waveguide briefly.

3.1. *Rectangular Waveguide Fields and Power Handling Capacities*

A rectangular waveguide of larger dimension a shorter dimension b is shown in figure 3-3, along with a set of rectangular coordinates (x, y, z). The waveguide is assumed to be evacuated (i.e., $\mu_r = \varepsilon_r = 1$). The $H_{m,n}$ modes have the following fields [8].

$$H_z = H_0 \cos(k_x x)\cos(k_y y) \tag{3.7}$$

$$H_x = H_0 \left[\frac{j\beta k_x}{k_{c_{m,n}}^2}\right] \sin(k_x x)\cos(k_y y) \tag{3.8}$$

$$H_y = H_0 \left[\frac{j\beta k_y}{k_{c_{m,n}}^2}\right] \cos(k_x x)\sin(k_y y) \tag{3.9}$$

$$E_x = \left[\frac{j\omega\mu k_y}{k_{c_{m,n}}^2}\right] H_0 \cos(k_x x)\sin(k_y y) \tag{3.10}$$

$$E_y = \left[\frac{-j\omega\mu k_x}{kyukc_{m,n}^2}\right] H_0 \sin(k_x x)\cos(k_y y) \tag{3.11}$$

$$E_z = 0 \tag{3.12}$$

where

$$\beta = k\left[1 - \frac{\omega_c^2}{\omega^2}\right]^{1/2} \quad ; \quad k = \frac{\omega}{c} \quad ; \quad k_c = \frac{\omega_c}{c} \tag{3.13}$$

$$k_x = \frac{m\pi}{a} \quad , \quad k_y = \frac{n\pi}{b} \quad ; \quad k_c^2 = k_x^2 + k_y^2 \tag{3.14}$$

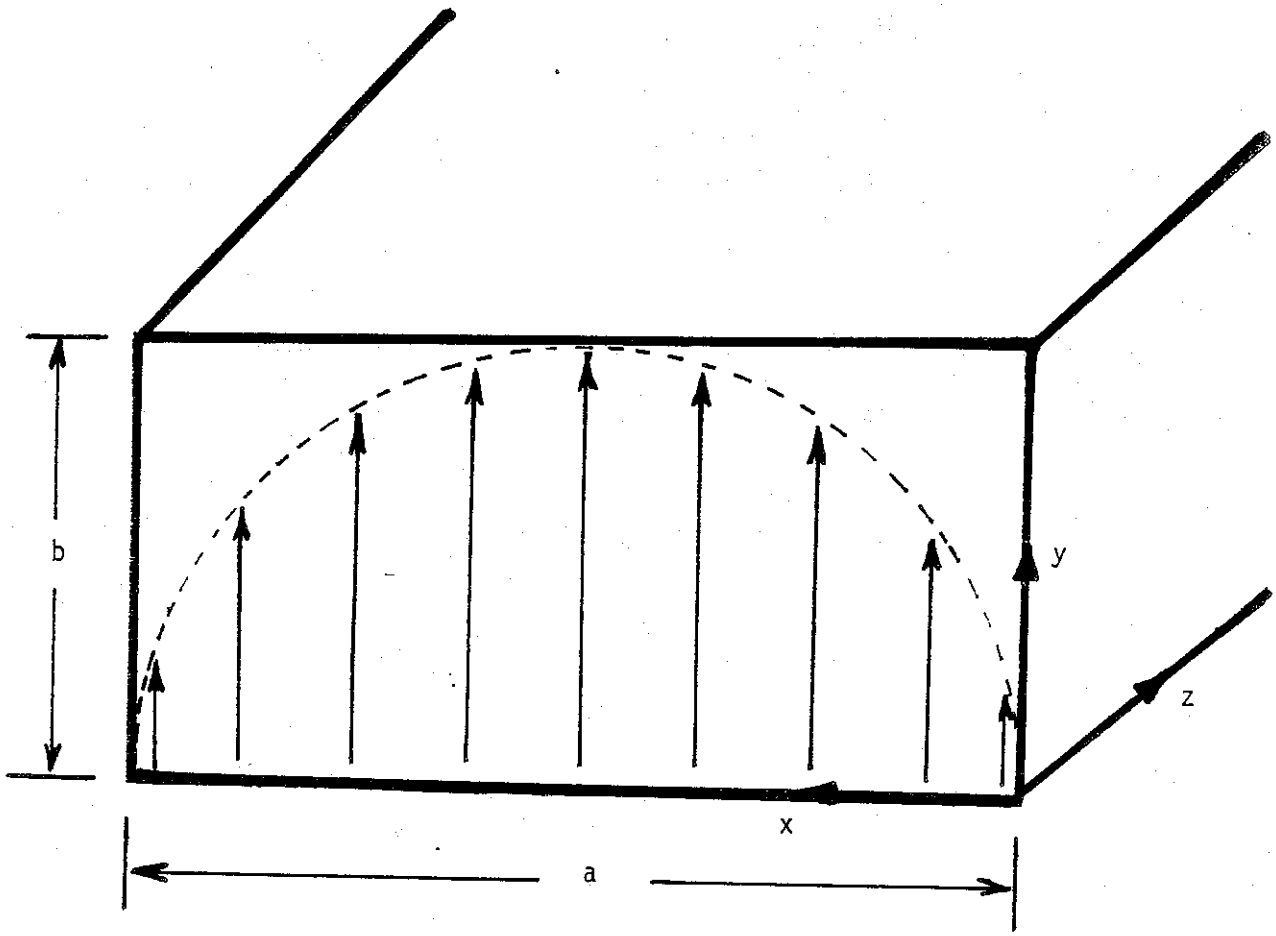

Figure 3-3. Cross section of a rectangular waveguide showing a $H_{1,0}$ mode of propagation

$$E_y = E_o \sin(\pi x/a)$$

Note that all field components are derivable from the axial magnetic field H_z. If we specialize the above fields for the dominant $H_{1,0}$ mode of propagation, we can write the $H_{1,0}$ fields as:

$$H_z = H_0 \cos\left[\frac{\pi x}{a}\right]$$

$$E_y = \frac{-j\omega\mu a}{\pi} H_0 \sin\left[\frac{\pi x}{a}\right] \tag{3.15}$$

$$H_x = \frac{j\beta a}{\pi} H_0 \sin\left[\frac{\pi x}{a}\right]$$

with the remaining components i.e., H_y, E_x and E_z being zero. The above field components can also be written as:

$$E_y = -Z_{1,0} H_x = E_0 \sin\left[\frac{\pi x}{a}\right] \tag{3.16}$$

$$H_z = j \frac{E_p}{Z_0} \left[\frac{\lambda}{2a}\right] \cos\left[\frac{\pi x}{a}\right] \tag{3.17}$$

where

$$E_0 = \frac{-j\omega\mu a H_0}{\pi} = \frac{-j2Z_0 a H_0}{\lambda}$$

$$Z_{1,0} = Z_0 \left[1 - \left[\frac{\lambda}{2a}\right]^2\right]^{-1/2} \tag{3.18}$$

$$Z_0 = \left[\frac{\mu_0}{\varepsilon_0}\right]^{1/2}, \quad \lambda = \frac{c}{f}$$

We can now compute the average power transferred by the propagating wave from the Poynting theorem (see 3.5),

$$
\begin{aligned}
P_{avg} &= \frac{1}{2}\ \text{Real} \int_0^a \int_0^b (-E_y H_x^*)\, dx\ dy \\
&= \frac{1}{2Z_{1,0}}\, E_0^2\, b \int_0^a \sin^2\left[\frac{\pi x}{a}\right] dx \\
&= E_0^2\, \frac{ab}{4Z_{1,0}} \\
&= \frac{E_0^2}{Z_0}\, \frac{ab}{4} \left[1 - \left[\frac{\lambda}{2a}\right]^2\right]^{1/2} \text{Watts}
\end{aligned}
\tag{3.19}
$$

The above expression P_{avg} is the average power transferred in the waveguide propagating a $H_{1,0}$ mode. Note that the peak power in the above waveguide is

$$
P_{peak} = 2P_{avg} = \frac{E_0^2}{Z_0}\, \frac{ab}{2} \left[1 - \left[\lambda/2a\right]^2\right]^{1/2} \tag{3.20}
$$

The above equation can be used in two different ways. For example, for a specified frequency, waveguide dimensions and the peak electric field E_0 (related to breakdown issue), one can compute the P_{peak} in Watts, which tells us the peak value of power that can be handled by the waveguide. On the other hand, for a given P_{peak}, waveguide dimensions and the frequency, one can estimate E_0 which is the peak electric field in the waveguide, which in turn specifies the level of vacuum. The ultimate limit of this process or the maximum power handled by the rectangular waveguide is limited by field emission from the metallic walls. This limit is discussed briefly in the next section.

Returning to (3.20), we have illustrated the power estimates using this equation by two examples in Tables 4 and 5. WR-975 and WR-340 are chosen for propagating 1 and 3 GHz HPM respectively [9,10]. If other frequencies are considered, suitable rectangular waveguide could be chosen for those frequencies. The inside dimensions, cut off frequencies for $H_{1,0}$ and the higher $H_{0,1}$ or $H_{2,0}$ modes are also indicated in these tables. There is also a short list of E_0 and P_{peak} in each of these tables, which is to be interpreted as follows. If the peak field in the $H_{1,0}$ mode is E_0(in MV/m), the peak power that this particular waveguide (WR-975 in Table 4 and WR-340 in Table 5) can handle is given by the listed value of P_{peak}. The peak E_0 field is governed by vacuum level in the waveguide. It is also noted that the P_{peak} values reported in Tables 4 and 5; for a prescribed value of the peak electric field E_0, are theoretical maxima and in practice P_{peak} values will be somewhat less owing to such factors as mechanical tolerances, surface deformities etc. In other words, the listed P_{peak} values are the idealized maxima values.

3.2. *Field Emission Limiting the Peak Electric Fields in Waveguides*

TABLE 4. 1 GHz Rectangular Waveguide

Designation	WR 975 or RG-204/U
	WR-4 (British Standard)
	153.IEC (R9)
Inside Dimensions	a = 247.65 mm; b = 123.83 mm
λ_c $(TE_{1,0})$	0.4953 m
f_c $(TE_{1,0})$	605.69 MHz
f_c $(TE_{0,1}) = f_c(TE_{2,0})$	1.2114 GHz
Nominal frequency range	0.75 to 1.12 GHz (for dominant mode operation)
Operating frequency	1 GHz
Operating wavelength	0.3 m

$E_0(MV/m)$	P_{peak}
1	32.3 MW
3	290.7 MW
10	3.23 GW
20	12.91 GW
30	29.0 GW
50	80.72 GW
100	0.32 TW

TABLE 5. 3 GHz Rectangular Waveguide

Designation	WR 340 or RG-112/U
	WG-9A (British Standard)
	153.IEC (R2B)
Inside Dimensions	a = 86.36 mm ; b = 43.18 mm
$\lambda_c(TE_{1,0})$	0.1727 m
$f_c(TE_{1,0})$	1.737 GHz
$f_c(TE_{0,1}) = f_c(TE_{2,0})$	3.474 GHz
Normal frequency range	2.20 to 3.30 GHz (for dominant mode operation)
Operating frequency	3 GHz
Operating wavelength	0.1 m

$E_0(MV/m)$	P_{peak}
1	4.03 MW
3	36.31 MW
10	403 MW
20	1.61 GW
30	3.63 GW
50	10.08 GW
100	40.3 GW
200	0.161 TW

Field emission is defined as the emission of electrons from the surface of a condensed phase into another phase, usually a vacuum under the action of high (3.0 to 6.0 GV/m) electrostatic fields [11]. In the present context, we are concerned with emissions of electrons from the metallic surfaces of the waveguides into the vacuum. Quantum mechanically, this phenomenon consists of the tunneling of electrons through the deformed potential barrier at the surface. This is in contrast with photo or thermionic emissions where the electrons with sufficient energies to go over the potential barrier, are emitted.

Another phenomenon termed the field ionization is closely related to field emission. In field ionization, electrons tunnel from atoms or molecules under the influence of high fields, typically in the range of 20 to 50 GV/m. Since these levels are an order of magnitude higher than the required field levels for field emission, we are not concerned with field ionization in the HPM context. Field emission then becomes the limiting factor of what is the maximum electric field that can be supported in a waveguide. It is implied that field emitted electrons lead to breakdown in waveguides and hence the electric fields in the waveguide must be well below the field levels required for field emission to start.

Although in general, electrostatic fields of the order of 3 to 6 GV/m are considered to be the levels required for field emission, in practice the frequency, pulse duration and surface conditions are all factors that influence the field emission threshold levels. The surface potential configuration or the surface condition itself affects the field emisison profoundly. So, in practical waveguides, the field emission may start at levels lower than a GV/m, owing to metallic surface condition. Whatever this level is, it is the limiting factor in the power handling capability of the waveguide.

In concluding this Section 3, we note that we have briefly investigated the power handling capacity of rectangular waveguides when the dominant mode ($H_{1,0}$) is propagating in them. The waveguides are operated at a frequency slightly lower than the cut off frequency of the next higher order mode, i.e., $H_{0,1}$ or $H_{2,0}$ which both have a cut off frequency twice that of the dominant $H_{1,0}$ mode.

For a prescribed peak electric field (of the $H_{1,0}$ mode) in the waveguide, one can estimate the peak power that can be transferred in the waveguide at a prescribed frequency. Two illustrative cases are considered at frequencies 1 GHz and 3 GHz. WR-975 and WR-340 are the recommended waveguides for these frequencies of operation. In both cases, the peak powers that can be handled in these waveguides for a given peak electric field are estimated and tabulated. The peak electric field that can be supported in the waveguide is a function of the level of vacuum. It is emphasized that the power handling capacity evaluated here are for idealized conditions. In practice, these powers are not reached in the waveguides but they only indicate the theoretical maximum of peak power that can be handled.

The ultimate limit on the peak electric field E_0 is the level required for field emission from the metallic surfaces of the waveguides. This phenomenon is briefly discussed and it is indeed the limiting factor for the power handling capacity of waveguides.

4. Near and Far Fields from an EM Pyramidal Horns

Rectangular waveguides operating in their fundamental $H_{1,0}$ mode are often used in propagating the microwave power from the source to the antenna. As discussed earlier, the waveguide is operated at a frequency just below the cut off frequency of the next $H_{0,1}$ and $H_{2,0}$ modes, both having the same cut off frequency. This assures maximum power handling capability in the waveguide. In the reflector antenna system under consideration, the HPM carrying waveguides are connected to a pyramidal horn via a suitable flange. It then is useful to know the electromagnetic fields near and far from the mouth of the horn. Near fields are useful in designing a dielectric interface from vacuum to air. Far fields are required to determine the illumination fields for the reflector (or subreflector) antenna.

In this paper, we write out the near and far fields and develop computer routines for their evaluation. The quadrature phase in the dominant mode is introduced [12], to account for the effect of the horn flare. The horn under consideration is a pyramidal horn, which is flared in both E and H planes. The E and H plane sectoral horns have a sharp beam in one plane, but a wide beam in the orthogonal plane. In order to obtain directivity in both E and H planes, the pyramidal horn is useful [13] while the two flare angles are independently adjustable.

In the following subsection, we consider the field radiated from a pyramidal horn.

4.1. *Fields from a Radiating Aperture*

A general aperture located in the $z = 0$ plane is shown in figure 4-1. Let the aperture electric field E be designated by an amplitude function A and a phase function Ψ, according as

$$\vec{E}(x',y') = \vec{\xi}(x',y')\, e^{-j\Psi(x',y')} \tag{4.1}$$

Assuming that the tangential electric field (- equivalently the magnetic current in the aperture) is zero everywhere in the $z = 0$ plane except over the aperture surface S_a, one can write the electric field at any observer location (x,y,z) as

$$\vec{E}(x,y,z) = \frac{1}{4\pi} \int_{S_a} dx' \int dy' \vec{E}(x',y') \left[\left(jk + \frac{1}{r} \right) \vec{1}_z \cdot \vec{1}_r + jk\, \vec{1}_z \cdot \vec{1}_s \right] \frac{e^{-jkr}}{r} \tag{4.2}$$

where

$\vec{k}$ ≡ free space wave number = $(2\pi/\lambda)$
$\vec{1}_z$ ≡ unit vector along the z direction
$\vec{1}_r$ ≡ unit vector along the r direction (figure 4-1)
$\vec{1}_s$ ≡ unit vector along a ray with components related to the phase function

The right half space $(z > 0)$ can be divided into 3 regions, namely (a) reactive near field, (b) radiating intermediate or Fresnel region and (c) radiating far field or

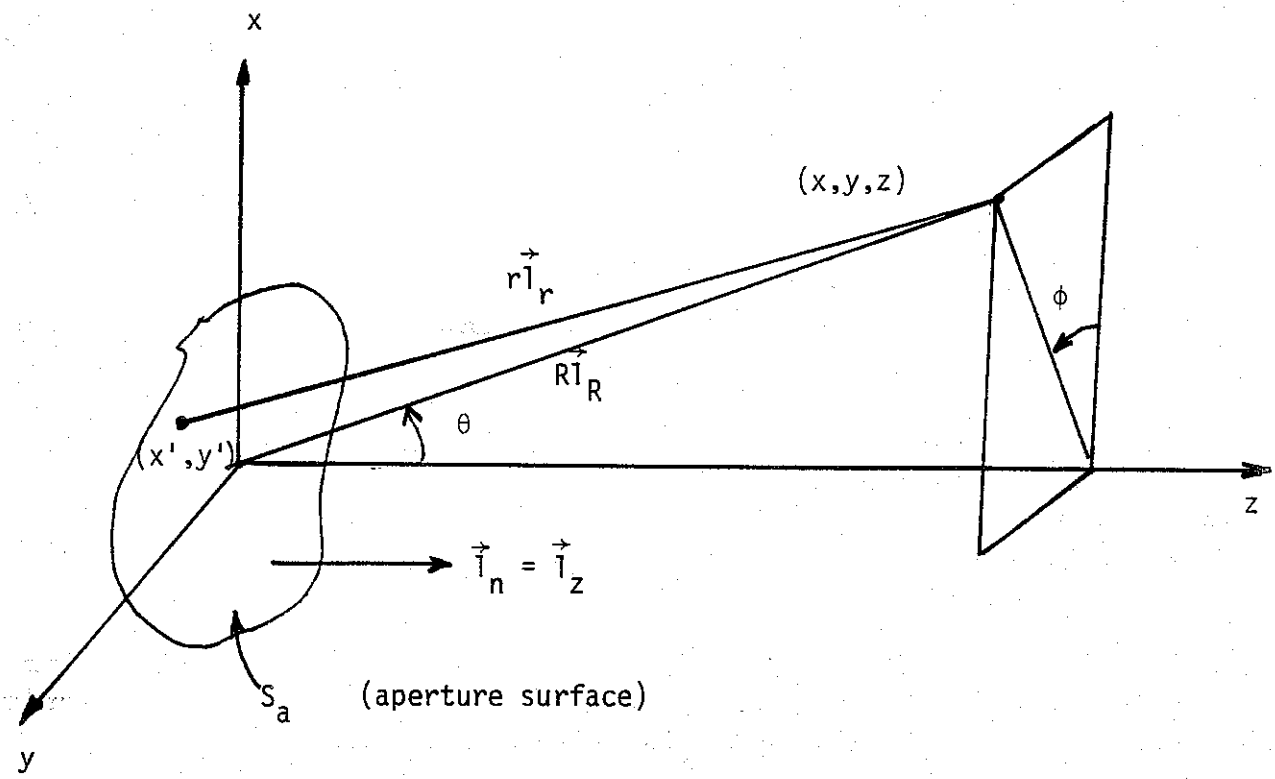

Figure 4-1. A radiating aperture located in z = 0 plane.

Fraunhofer region. The regions are mathematically characterized as follows

(a) Reactive (non-radiating) region

No approximations are possible and indeed the integral representation itself is somewhat approximate.

(b) Fresnel region

$$(\frac{1}{r}) \ll |jk| \tag{4.3a}$$

$$(\vec{1}_z \cdot 1_r) \simeq (\vec{1}_z \cdot \vec{1}_R)\cos(\theta) \tag{4.3b}$$

$$\frac{1}{r} = \frac{1}{R} \quad \text{in the amplitude factor} \tag{4.3c}$$

$$\begin{aligned} r &= \left[(x-x')^2 + (y-y')^2 + z^2\right]^{1/2} \\ &\simeq z + \frac{(x-x')^2}{2z} + \frac{(y-y')^2}{2z} \end{aligned} \tag{4.3d}$$

in the phase factor exp(-jkr)

(c) Fraunhofer region

Same as (4.3a), (4.3b), and (4.3c) but the "r" in the phase factor can now be approximated by

$$\begin{aligned} r &= \left[(x-x')^2 + (y-y')^2 + z^2\right]^{1/2} \\ &= \left[x^2 + y^2 + z^2 + (x'^2+y'^2) - 2xx' - 2yy'\right]^{1/2} \\ &= R - \frac{(xx'+yy')}{R} \end{aligned} \tag{4.4}$$

where $R^2 = x^2 + y^2 + z^2$

Typically, the (non-radiating) reactive zone extends from the mouth of the aperture to a wavelength or so. The Fresnel fields are of interest for the design of the dielectric interface and certainly the far fields (Fraunhofer) zone are also of interest to precisely determine the reflector illumination. The classical approximations noted above are applied to a pyramidal horn aperture in the next section in evaluating the

Fresnel and Fraunhofer fields.

4.2. *Fresnel Fields from a Pyramidal Horn*

A schematic of a pyramidal horn is shown in figure 4-2, along with a set of cartesian (x,y,z) and spherical (R,θ,ϕ) coordinate systems. a and b are the dimensions of the aperture in the $z = 0$ plane. l_E and l_H are the E and H plane slant heights as indicated in figure 4-2.

Assuming the field at the aperture of the transmitting horn is the same as though the horn were continued, the aperture distribution can be written as [14]

$$\vec{1}_x \cdot \vec{E}(x',y') = E_0 \cos\left[\frac{\pi y}{a}\right] e^{-jk\left[\frac{x'^2}{2l_E} + \frac{y'^2}{2l_H}\right]} \tag{4.5}$$

Consequently, in the Fresnel approximation (4.3a to 4.3d),

$$\vec{E}(x,y,z) = \frac{1}{4\pi} \iint \vec{E}(x',y') \frac{e^{-jkr}}{r} \left[\left[jk + \frac{1}{r}\right]\cos(\theta) + jk\right] dx'dy'$$

becomes

$$\vec{E}(x,y,z) \simeq jk\left[1 + \cos(\theta)\right] \frac{e^{-jkz}}{4\pi z} \iint \vec{E}(x',y')\, e^{-jk\left\{z + \frac{(x-x')^2}{2z} + \frac{(y-y')^2}{2z}\right\}} dx'\, dy'$$

Since the aperture field is x-directed, we have

$$\begin{aligned} E_x(x,y,z) &\simeq j \frac{E_0}{2\lambda z}\left[1 + \cos(\theta)\right] e^{-jkz} \int_{-b/2}^{b/2} dx' \int_{-a/2}^{a/2} \\ &\quad \cos\left[\frac{\pi y'}{a}\right] e^{-jk\left\{\frac{x'^2}{2l_E} + \frac{y'^2}{2l_H}\right\}} e^{-jk\left\{\frac{(x-x')^2}{2z} + \frac{(y-y')^2}{2z}\right\}} \\ &= \frac{jE_0}{2\lambda z}\left[1 + \cos(\theta)\right] e^{-jkz} \int_{-b/2}^{b/2} dx'\, e^{-jk\left\{\frac{x'^2}{2l_E} + \frac{(x-x')^2}{2z}\right\}} \\ &\quad \int_{-a/2}^{a/2} dy' \cos\left[\frac{\pi y'}{a}\right] e^{-jk\left\{\frac{y'^2}{2h_H} + \frac{(y-y')^2}{2z}\right\}} \end{aligned} \tag{4.6}$$

We observe that the Fresnel field is maximum on the axis i.e., $x = y = 0$, $\theta = 0$ and

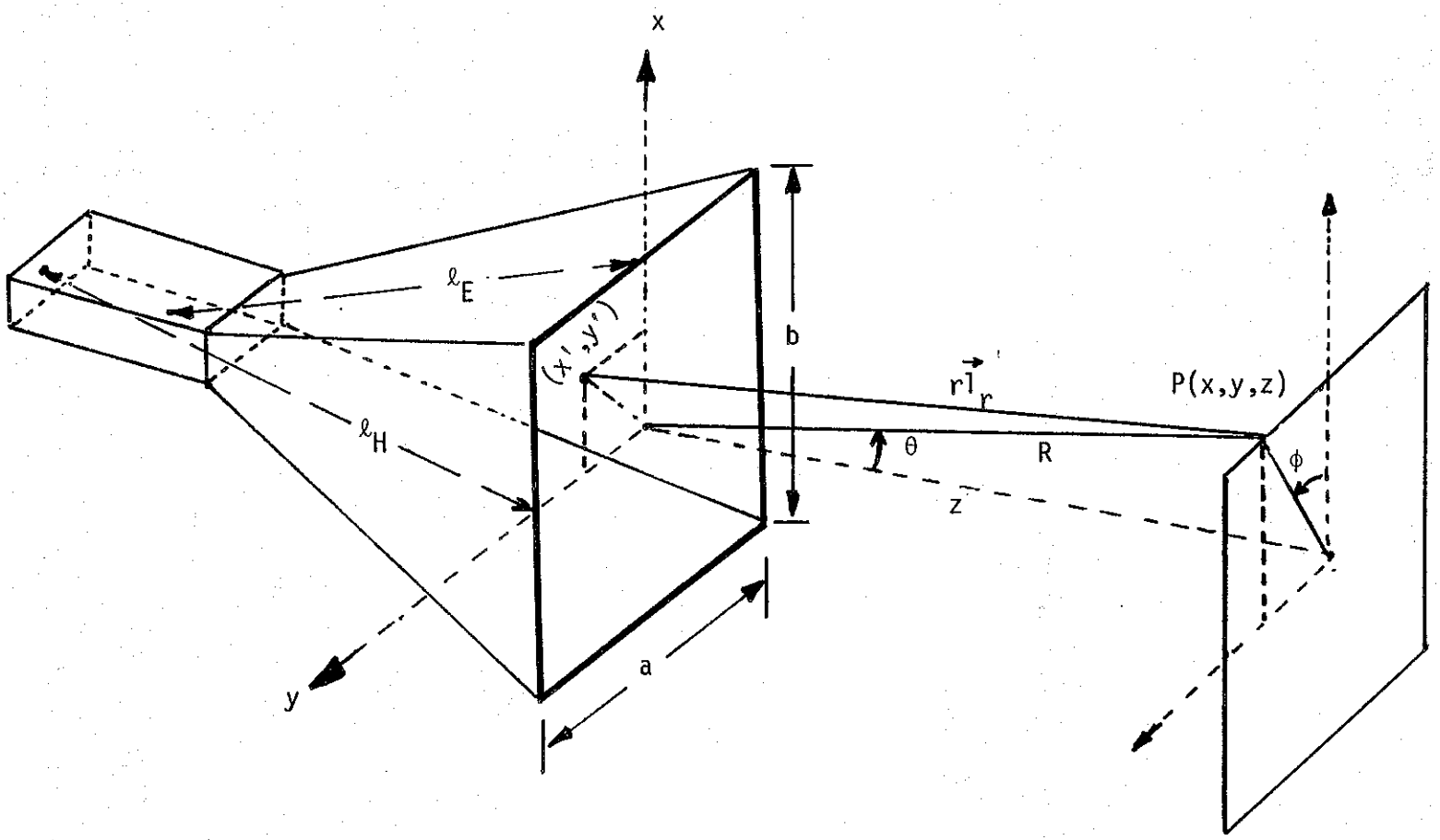

Figure 4-2. A transmitting pyramidal horn.

that we are interested in the field magnitude from a breakdown point of view. For these reasons, we can set $x = y = \theta = 0$ and then take magnitudes of both sides of the above equation, resulting in

$$
\begin{aligned}
|E_x(0,0,z)| \simeq \frac{E_0}{2\lambda z} \Bigg| & \int_{-b/2}^{b/2} dx' \, e^{-jk\left\{\frac{1}{2l_E}+\frac{1}{2z}\right\}x'^2} \\
& \int_{-a/2}^{a/2} \left\{ e^{\frac{j\pi y'}{a}} + e^{\frac{-j\pi y'}{a}} \right\} \left[e^{-jk\left\{\frac{1}{2l_h}+\frac{1}{2z}\right\}y'^2} \right] \Bigg| \\
= \frac{E_0}{2\lambda z} \Bigg| & \int_{-b/2}^{b/2} dx' \, e^{-j\frac{\pi}{2}(\sqrt{\alpha}x')^2} \Bigg| \\
& \left| \int_{-a/2}^{a/2} dy' \, e^{-j\frac{\pi}{2}\left\{\beta y'^2 - \frac{2y'}{a}\right\}} + \int_{-a/2}^{a/2} dy' \, e^{-j\frac{\pi}{2}\left\{\beta y'^2 + \frac{2y'}{a}\right\}} \right|
\end{aligned}
\tag{4.7}
$$

where

$$\alpha = \frac{2}{\lambda}\left\{\frac{1}{l_E}+\frac{1}{z}\right\} = \frac{2\left[l_E+z\right]}{\lambda l_E z} \tag{4.8a}$$

$$\beta = \frac{2}{\lambda}\left\{\frac{1}{l_H}+\frac{1}{z}\right\} = \frac{2(l_H+z)}{\lambda l_H z} \tag{4.8b}$$

We need to make a change of variable $\sqrt{\alpha}\,x' = u$ and also complete the squares in the exponent of the y' integrals, in order to be able to write the above expression in compact form, resulting in

$$
\begin{aligned}
E_x(0,0,z) \simeq \frac{E_0}{2\lambda z}\frac{1}{\sqrt{\alpha}} & \left| \int_{u_1}^{u_2} du \, e^{-j\frac{\pi}{2}u^2} \right| \\
& \left| e^{j\frac{\pi}{2}\frac{1}{a^2\beta}} \left[\int_{-a/2}^{a/2} dy' \, e^{-j\frac{\pi}{2}\left\{\sqrt{\beta}\,y' - \frac{1}{a\sqrt{\beta}}\right\}^2} + \int_{-a/2}^{a/2} dy' \, e^{-j\frac{\pi}{2}\left\{\sqrt{\beta}\,y' + \frac{1}{a\sqrt{\beta}}\right\}^2} \right] \right|
\end{aligned}
\tag{4.9}
$$

Making the following change of variables,

$$\left[\sqrt{\beta}\, y' - \frac{1}{a\sqrt{\beta}}\right] = v \tag{4.10a}$$

$$\left[\sqrt{\beta}\, y' + \frac{1}{a\sqrt{\beta}}\right] = w \tag{4.10b}$$

we get

$$E_x(0,0,z)$$

$$\simeq \frac{E_0}{2\lambda z}\,\frac{1}{\sqrt{\alpha\beta}}\left|\int_{u_1}^{u_2} du\; e^{-j\frac{\pi}{2}u^2}\left[\int_{v_1}^{v_2} dv\; e^{-j\frac{\pi}{2}v^2} + \int_{w_1}^{w_2} dw\; e^{-j\frac{\pi}{2}w^2}\right]\right| \tag{4.11}$$

where the limits of integrals are given by

$$u_1 = -\frac{b}{2}\sqrt{\alpha} = -\frac{b}{2}\sqrt{\frac{2}{\lambda}\left[\frac{1}{l_E} + \frac{1}{z}\right]} = -\sqrt{\frac{b^2(l_E+z)}{2\lambda l_E z}} \tag{4.12a}$$

$$u_2 = -u_1 = \sqrt{\frac{b^2(l_E+z)}{2\lambda l_E z}} \tag{4.12b}$$

$$v_1 = -\frac{1}{\sqrt{2}}\left[\sqrt{\frac{a^2(l_H+z)}{\lambda l_H z}} + \sqrt{\frac{\lambda l_H z}{a^2(l_H+z)}}\right] \tag{4.13a}$$

$$v_2 = \frac{1}{\sqrt{2}}\left[\sqrt{\frac{a^2(l_H+z)}{\lambda l_H z}} - \sqrt{\frac{\lambda l_H z}{a^2(l_H+z)}}\right] \tag{4.13b}$$

$$w_1 = -\frac{1}{\sqrt{2}}\left[\sqrt{\frac{a^2(l_H+z)}{\lambda l_H z}} - \sqrt{\frac{\lambda l_H z}{a^2(l_H+z)}}\right] \tag{4.14a}$$

$$w_2 = \frac{1}{\sqrt{2}} \left[\sqrt{\frac{a^2(l_H+z)}{\lambda l_H z}} + \sqrt{\frac{\lambda l_H z}{a^2(l_H+z)}} \right] \tag{4.14b}$$

Observe that

$$v_1 = -w_2 \quad \text{and} \quad v_2 = -w_1 \tag{4.15}$$

Using (4.15) in (4.11), we have

$$\begin{aligned} E_x(0,0,z) &\simeq \frac{E_0}{2\lambda z} \frac{1}{\sqrt{\alpha\beta}} \left| \int_{v_1}^{v_2} du\ e^{-j(\pi/2)u^2} \left[\int_{v_1}^{v_2} dv\ e^{-j(\pi/2)v^2} + \int_{-v_2}^{-v_1} dw\ e^{-j(\pi/2)w^2} \right] \right| \\ &= \frac{E_0}{\lambda z} \frac{1}{\sqrt{\alpha\beta}} \left| \int_{u_1}^{u_2} e^{-j(\pi/2)u^2} du \times \int_{v_1}^{v_2} e^{-j(\pi/2)v^2} dv \right| \end{aligned} \tag{4.16}$$

The integrals can be written in Fresnel form by noting

$$\begin{aligned} \int_{\xi_1}^{\xi_2} e^{-j(\pi/2)\xi^2} d\xi &= \int_0^{\xi_2} e^{-j(\pi/2)\xi^2} d\xi - \int_0^{\xi_1} e^{-j(\pi/2)\xi^2} d\xi \\ &= [C(\xi_2) - C(\xi_1)] - j[S(\xi_2) - S(\xi_1)] \end{aligned} \tag{4.17}$$

Equation (4.16) after substitution for α and β from (4.8) becomes, $E_x(0,0,z)$

$$E_x(0,0,z) \simeq \frac{E_0}{2} \sqrt{\frac{l_E l_H}{(l_E+z)(l_H+z)}} \quad F_1(u) \quad F_2(v) \tag{4.18}$$

where

$$F_1(u) = \left\{ [C(u_2) - C(u_1)]^2 + [S(u_2) - S(u_1)]^2 \right\}^{1/2} \tag{4.19a}$$

$$F_2(v) = \left\{ [C(v_2) - C(v_1)]^2 + [S(v_2) - S(v_1)]^2 \right\}^{1/2} \tag{4.19b}$$

where the Fresnel integrals are defined by

$$C(\xi) = \int_0^{\xi} \cos\left[\frac{\pi}{2} x^2\right] dx \tag{4.20a}$$

$$S(\xi) = \int_0^{\xi} \sin\left[\frac{\pi}{2} x^2\right] dx \tag{4.20b}$$

Equation (4.18) can be rewritten in normalized form as follows

$$\begin{aligned} T(0,0,z) &= \left|\frac{E_x(0,0,z)}{E_0}\right| \equiv \text{dimensionless transfer function} \\ &= \frac{1}{2}\sqrt{\frac{l_E+l_H}{(l_E+z)(l_H+z)}}\, F_1(u)\ F_2(v) \end{aligned} \tag{4.21}$$

The above expression is indicative of how large the electric field along the axis is, compared to the peak electric field E_0 in the aperture. This is very useful information in designing the vacuum-air interface. Also, it is observed that $T(0,0,z)$ of (4.21) can be computed once a, b, l_E, l_H (horn parameters) and the distance z is specified. The above expression for $T(0,0,z)$ is in agreement with similar expressions available in classical literature and it is also readily computable. Some numerical results for illustrative purposes are reported later after a review of the Fraunhofer fields.

4.3. *Fraunhofer Fields from a Pyramidal Horn*

The quadratic phase corrected aperture field of (4.5) can once again be used in the far field (or Fraunhofer) computation for a pyramidal horn, along with the Fraunhofer conditions. However, the derivation is available in classical literature [1] and the results are summarized below. It is observed that the E-plane pattern of a pyramidal horn is the same as that of an E-plane sectoral horn and the H-plane pattern of a pyramidal horn is the same as that of a H-plane sectoral horn. Consequently, one can choose the E-plane parameters for a pyramidal horn by using the E-plane sectoral horn data and likewise for the H-plane. In practice, this procedure gives good results [1].

With reference to figure 4-2, we note that (R,θ,ϕ) is the spherical coordinate system under use and the E and H planes are characterized by

$$\phi = \pi/2 \qquad \text{(figure 4-2) for H-plane} \tag{4.22}$$

$$\phi = 0 \qquad \text{(figure 4-2) for E-plane} \tag{4.23}$$

In general there are 3 components of electric field i.e., E_R, E_θ, E_ϕ. In the Fraunhofer region, the radial component $E_R = 0$. We can write down [1], the far fields of H-

plane sectoral and E-plane sectoral horns and then specialize them for the pyramidal horn in the 2 planes

H-plane Sectoral Horn [eqn. 15.34 of Reference 1]

$$E_R = 0 \tag{4.24a}$$

$$E_\theta = \frac{jk\, e^{-jkR}}{4\pi R} [1 + cos(\theta)]\ cos(\phi)\, f_x \tag{4.24b}$$

$$E_\phi = \frac{-jk\, e^{-jkR}}{4\pi R} [1 + cos(\theta)]\ sin(\phi)\, f_x \tag{4.24c}$$

where

$$f_x = \frac{E_0 b}{2} \frac{\sin[(kb/2)cos(\phi)sin(\theta)]}{[(kb/2)cos(\phi)sin(\theta)]} I \tag{4.24d}$$

$$I = \sqrt{\frac{\pi l_H}{k}} \left\{ \exp\left[\frac{j[k\ \sin(\phi)\sin(\theta)+(\pi/2)]^2 l_H}{2k}\right] \left[C(\zeta_2)-C(\zeta_1) - jS(\zeta_2) + jS(\zeta_2)\right] \right. \tag{4.25}$$
$$\left. + \exp\left[\frac{j[k\ sin(\phi)\sin(\theta)-(\pi/2)]^2 l_H}{2k}\right] \left[C(\zeta_4) - C(\zeta_3) - jS(\zeta_4) + jS(\zeta_3)\right] \right\}$$

with i = 1, 2, 3, 4, are given by

$$\zeta_i = \sqrt{\frac{1}{\pi k l_H}} \left[(-1)^i\ \frac{ka}{a} - kl_H\ \sin(\phi)\sin(\theta) + \alpha_i\ \frac{\pi l_H}{a}\right] \tag{4.26}$$

E-plane Sectoral Horn

$E_R = 0$, E_θ and E_ϕ are same as in (4.23b) and (4.23c) except f_x is now given by

$$f_x = \frac{2E_0 \pi a\ \cos(k_y a/2)}{\pi^2 - k_y^2 a^2} \sqrt{\frac{\pi l_E}{k}}\ e^{jk_x^2 l_E/(2k)}\ I_1 \tag{4.27}$$

$$I_1 = \left[C(\xi_2) - C(\xi_1) - jS(\xi_2) + jS(\xi_1)\right] \tag{4.28}$$

where

$$k_x = k\ cos(\phi)\ sin(\theta) \tag{4.29a}$$

$$k_y = k\ \sin(\phi)\ \sin(\theta) \tag{4.29b}$$

$$\xi_i = \sqrt{\frac{1}{\pi k l_E}}\left[(-1)^i k\ \frac{a}{2} - k_x l_E\right] \quad \text{for } i = 1, 2 \tag{4.29c}$$

Now that the far fields of E and H plane sectoral horns are written above, we can write the H-plane and E-plane radiation patterns of a pyramidal horn by setting the conditions of equations (4.22) and (4.23) in above.

H-plane Radiation Pattern of a Pyramidal Horn

$$E_R = 0 \tag{4.30a}$$

$$E_\theta = 0 \tag{4.30b}$$

$$E_\phi = \frac{-j(kb)e^{-jkR}}{4\pi R}\ \frac{[1+cos(\theta)]}{2}\ E_0 \sqrt{\frac{\pi l_H}{k}}\ F_3(\theta,\zeta_i) \tag{4.30c}$$

where the function F_3 is given by

$$\begin{aligned} F_3(\theta,\zeta_i) = \Bigg\{ &\exp\left[j\left[k\ \sin\theta + \frac{\pi}{a}\right]^2 \frac{l_H}{2k}\right]\left[C(\zeta_2) - C(\zeta_1) - jS(\zeta_2) + jS(\zeta_3)\right] \\ &+ \exp\left[j\left[k\ \sin\theta - \frac{\pi}{a}\right]^2 \frac{l_H}{2k}\right]\left[C(\zeta_4) - C(\zeta_3) - jS(\zeta_4) + jS(\zeta_3)\right]\Bigg\} \end{aligned} \tag{4.31}$$

The ζ_i in above for i = 1, 2, 3, 4 are given by

$$\zeta_i = \sqrt{\frac{1}{\pi k l_H}}\left[(-1)^i\ \frac{ka}{2} - kl_H\ sin(\theta) + \alpha_i\ \frac{\pi l_H}{a}\right] \tag{4.32}$$

$$\alpha_i = -1 \quad \text{for} \quad i = 1, 2 \tag{4.33a}$$

$$\alpha_i = +1 \quad \text{for} \quad i = 3, 4 \tag{4.33b}$$

The above E_θ and E_ϕ are obtained by setting $\phi = \pi/2$ in (4.24) to (4.26).

E-plane Radiation Pattern of a Pyramidal Horn

$$E_R = 0 \tag{4.34a}$$

$$E_\phi = 0 \tag{4.34b}$$

$$E_\theta = \frac{jk\, e^{-jkR}}{4\pi R} \left[1 + cos\,(\theta)\right] \frac{2E_0 a}{\pi} \sqrt{\frac{\pi l_E}{k}}\, e^{jkl_E \sin^2(\theta)/2}\, F_4(\theta,\xi_i) \tag{4.34c}$$

with

$$F_4(\theta,\xi_i) = [C(\xi_2) - C(\xi_1) - jS(\xi_2) + jS(\xi_1)] \tag{4.35}$$

$$\xi_i = \sqrt{\frac{1}{\pi k l_E}} \left[(-1)^i \frac{ka}{2} - k\, sin\,(\theta)\, l_E\right] \quad \text{for} \quad i = 1, 2 \tag{4.36}$$

The above E_θ and E_ϕ are obtained by setting $\phi = 0$ in (4.24), (4.27) to (4.29).

Computer routines have been written to evaluate the near field as well as the H-plane and E-plane radiation patterns of a pyramidal horn and illustrative results are reported after some summarizing remarks.

In Section 4, the Fresnel field and the Fraunhofer fields in the E and H planes of a pyramidal electromagnetic horn are reviewed. The quadrature phase correction in the aperture is included to obtain accuracy in the computations, as opposed to using the principal mode waveguide field.

The Fraunhofer radiation patterns are quite well known in classical literature, but the Fresnel field computations performed here are considered to be essential in designing a vacuum-air interface. The objective in this note is to develop the computational tools to evaluate the electromagnetic fields. These and similar computations for the actual pyramidal horn selected in the HPM antenna system, will be used in future for the design of the interface. The pyramidal horn considered here is for numerical illustrative purpose and not intended to be the pyramidal horn that will be used in the entire system. At this stage, all the necessary computational tools are being developed

to aid in the design of the final system.

4.4. *Illustrative Example of Near Fields of a Pyramidal Horn*

In this subsection, we illustrate the computation of equation (4.21) for the normalized electric field along the axis, in the Fresnel region.

$$T_x(0,0,z) = \left| \frac{E_x(0,0,z)}{E_0} \right| = \frac{1}{2} \sqrt{\frac{l_E+l_H}{(l_E+z)(l_H+z)}}\, F_1(u)\; F_2(v) \tag{4.37}$$

where $F_1(u)$ and $F_2(v)$ are given in (4.18) and the various arguments u_1, u_2, v_1, and v_2 are given in (4.12) and (4.13).

The input quantities for evaluating T_x are a, b, l_E, l_H, and λ. T_x may then be computed using the routine FRESNEL as a function of normalized axial coordinate z_{NORM}, given by

$$z_{NORM} = z/ff \tag{4.38}$$

where ff is the conventional far field distance given by

$$ff = \frac{2d^2}{\lambda} = \frac{2(a^2+b^2)}{\lambda} \tag{4.39}$$

We have used for illustrative purposes the following two cases of pyramidal horns.

	Case 1	Case 2
a	1.433 m	0.600 m
b	1.059 m	0.450 m
l_E	1.900 m	3.000 m
l_H	1.972 m	3.000 m
λ	0.300 m	0.300 m

It is noted that the above cases are for numerical illustration only at this point. In future reports, on the system description, actual pyramidal horns at 1 and 3 GHz that will mate with the waveguides selected in earlier reports will be designed. Sample results for the above horns are presented in tables 6 to 9 and figures 4-3 and 4-4.

For the illustrative case considered here, it is seen that T(z) oscillates and then follows the (1/R) roll off in the far field. Knowing the aperture peak field E_0, curves and calculations such as these tell us precisely the maximum field in the Fresnel region

TABLE 6 FRESNEL INTEGRALS

Z	C(Z)	S(Z)
.1	.09999753	.00052359
.2	.19992110	.00418761
.3	.29940100	.01411700
.4	.39748070	.03335942
.5	.49234420	.06473242
.6	.58109550	.11054020
.7	.65965240	.17213640
.8	.72284410	.24934140
.9	.76482310	.33977630
1.0	.77989340	.43825910
1.1	.76380670	.53649800
1.2	.71543780	.62340090
1.3	.63855050	.68633340
1.4	.54309600	.71352520
1.5	.44526110	.69750490
1.6	.36546170	.63888780
1.7	.32382670	.54919590
1.8	.33363280	.45093850
1.9	.39447050	.37334720
2.0	.48825330	.34341560
2.1	.58156430	.37427320
2.2	.63628610	.45570470
2.3	.62656180	.55315170
2.4	.55496130	.61969020
2.5	.45741280	.61918200
2.6	.38893710	.54998910
2.7	.39249380	.45291740
2.8	.46749150	.39152820
2.9	.56237700	.41014050
3.0	.60572100	.49631300
3.1	.56159400	.58181620
3.2	.46631990	.59334990
3.3	.40569420	.51928620
3.4	.43849170	.42964900
3.5	.53257260	.41524760
3.6	.58795380	.49230970
3.7	.54194590	.57498070
3.8	.44809510	.56561900
3.9	.42233230	.47520210
4.0	.49842620	.42051520
4.1	.57369620	.47579780
4.2	.54171940	.56319950
4.3	.44944020	.55399630
4.4	.43833270	.46226700
4.5	.52602620	.43427280
4.6	.56723740	.51619270
4.7	.49142680	.56714580
4.8	.43379630	.49675030
4.9	.50016070	.43506650
5.0	.56363260	.49919250

Fresnel Integrals

Definition

$$C(z)=\int_0^z \cos\left(\frac{\pi}{2}t^2\right)dt$$

$$S(z)=\int_0^z \sin\left(\frac{\pi}{2}t^2\right)dt$$

TABLE 7 FRESNEL INTEGRALS

Z	C(Z)	S(Z)
-.1	-.09999753	-.00052359
-.2	-.19992110	-.00418761
-.3	-.29940100	-.01411700
-.4	-.39748070	-.03335942
-.5	-.49234420	-.06473242
-.6	-.58109550	-.11054020
-.7	-.65965240	-.17213640
-.8	-.72284410	-.24934140
-.9	-.76482310	-.33977630
-1.0	-.77989340	-.43825910
-1.1	-.76380670	-.53649800
-1.2	-.71543780	-.62340090
-1.3	-.63855050	-.68633340
-1.4	-.54309600	-.71352520
-1.5	-.44526110	-.69750490
-1.6	-.36546170	-.63888780
-1.7	-.32382670	-.54919590
-1.8	-.33363280	-.45093850
-1.9	-.39447050	-.37334720
-2.0	-.48825330	-.34341560
-2.1	-.58156430	-.37427320
-2.2	-.63628610	-.45570470
-2.3	-.62656180	-.55315170
-2.4	-.55496130	-.61969020
-2.5	-.45741280	-.61918200
-2.6	-.38893710	-.54998910
-2.7	-.39249380	-.45291740
-2.8	-.46749150	-.39152820
-2.9	-.56237700	-.41014050
-3.0	-.60572100	-.49631300
-3.1	-.56159400	-.58181620
-3.2	-.46631990	-.59334990
-3.3	-.40569420	-.51928620
-3.4	-.43849170	-.42964900
-3.5	-.53257260	-.41524760
-3.6	-.58795380	-.49230970
-3.7	-.54194590	-.57498070
-3.8	-.44809510	-.56561900
-3.9	-.42233230	-.47520210
-4.0	-.49842620	-.42051520
-4.1	-.57369620	-.47579780
-4.2	-.54171940	-.56319950
-4.3	-.44944020	-.55399630
-4.4	-.43833270	-.46226700
-4.5	-.52602620	-.43427280
-4.6	-.56723740	-.51619270
-4.7	-.49142680	-.56714580
-4.8	-.43379630	-.49675030
-4.9	-.50016070	-.43506650
-5.0	-.56363260	-.49919250

Fresnel Integrals

Definition

$$C(z)=\int_0^z \cos\left(\frac{\pi}{2}t^2\right)dt$$

$$S(z)=\int_0^z \sin\left(\frac{\pi}{2}t^2\right)dt$$

FRESNEL CASE # 1

A= 1.43300 B= 1.05900 LE= 1.80000 LH= 1.97200
LAMDA= .3000 #SAMPLES= 100

Z	LOG Z	T(Z)
.0100	-2.0000	1.0437600
.0107	-1.9700	1.0440830
.0115	-1.9400	.9646524
.0123	-1.9100	.8517883
.0132	-1.8800	.7646524
.0141	-1.8500	.7521484
.0151	-1.8200	.8097016
.0162	-1.7900	.8949659
.0174	-1.7600	.9685788
.0186	-1.7300	1.0074450
.0200	-1.7000	1.0053550
.0214	-1.6700	.9689344
.0229	-1.6400	.9104071
.0245	-1.6100	.8413629
.0263	-1.5800	.7703686
.0282	-1.5500	.7036683
.0302	-1.5200	.6464850
.0324	-1.4900	.6031515
.0347	-1.4600	.5760615
.0372	-1.4300	.5646882
.0398	-1.4000	.5658652
.0427	-1.3700	.5752460
.0457	-1.3400	.5887957
.0490	-1.3100	.6035338
.0525	-1.2800	.6175737
.0562	-1.2500	.6298455
.0603	-1.2200	.6397805
.0646	-1.1900	.6470867
.0692	-1.1600	.6516153
.0741	-1.1300	.6532980
.0794	-1.1000	.6521282
.0851	-1.0700	.6481575
.0912	-1.0400	.6414942
.0977	-1.0100	.6322994
.1047	-.9800	.6207802
.1122	-.9500	.6071792
.1202	-.9200	.5917608
.1288	-.8900	.5748020
.1380	-.8600	.5565798
.1479	-.8300	.5373632
.1585	-.8000	.5174065
.1698	-.7700	.4969458
.1820	-.7400	.4761938
.1950	-.7100	.4553407
.2089	-.6800	.4345520
.2239	-.6500	.4139708
.2399	-.6200	.3937173
.2570	-.5900	.3738917
.2754	-.5600	.3545752
.2951	-.5300	.3358321
.3162	-.5000	.3177117
.3388	-.4700	.3002503
.3631	-.4400	.2834727
.3890	-.4100	.2673941
.4169	-.3800	.2520210
.4467	-.3500	.2373534
.4786	-.3200	.2233853

TABLE 8

Fresnel field along the axis, normalized to the peak aperture field E_0

CASE # 1

TABLE 8 Continued and Concluded

.5129	-.2900	.2101058
.5495	-.2600	.1975007
.5888	-.2300	.1855522
.6310	-.2000	.1742404
.6761	-.1700	.1635439
.7244	-.1400	.1534398
.7762	-.1100	.1439042
.8318	-.0800	.1349130
.8913	-.0500	.1264420
.9550	-.0200	.1184669
1.0233	.0100	.1109635
1.0965	.0400	.1039084
1.1749	.0700	.0972784
1.2589	.1000	.0910512
1.3490	.1300	.0852051
1.4454	.1600	.0797191
1.5488	.1900	.0745731
1.6596	.2200	.0697478
1.7783	.2500	.0652248
1.9055	.2800	.0609866
2.0417	.3100	.0570162
2.1878	.3400	.0532979
2.3442	.3700	.0498163
2.5119	.4000	.0465574
2.6915	.4300	.0435074
2.8840	.4600	.0406535
3.0903	.4900	.0379836
3.3113	.5200	.0354862
3.5481	.5500	.0331507
3.8019	.5800	.0309667
4.0738	.6100	.0289248
4.3652	.6400	.0270160
4.6774	.6700	.0252317
5.0119	.7000	.0235641
5.3703	.7300	.0220057
5.7544	.7600	.0205494
6.1659	.7900	.0191887
6.6069	.8200	.0179174
7.0795	.8500	.0167297
7.5858	.8800	.0156203
8.1283	.9100	.0145840
8.7096	.9400	.0136160
9.3325	.9700	.0127119
10.0000	1.0000	.0118676

FRESNEL CASE # 2

A= .60000 B= .45000 LE= 3.00000 LH= 3.00000
LAMDA= .3000 #SAMPLES= 100

Z	LOG Z	T(Z)
.0100	-2.0000	.9025024
.0107	-1.9700	.8147243
.0115	-1.9400	.7114684
.0123	-1.9100	.6722688
.0132	-1.8800	.7256542
.0141	-1.8500	.8247301
.0151	-1.8200	.9116592
.0162	-1.7900	.9529833
.0174	-1.7600	.9432185
.0186	-1.7300	.8953950
.0200	-1.7000	.8270246
.0214	-1.6700	.7524932
.0229	-1.6400	.6840045
.0245	-1.6100	.6339220
.0263	-1.5800	.6121986
.0282	-1.5500	.6207710
.0302	-1.5200	.6528060
.0324	-1.4900	.6983755
.0347	-1.4600	.7496613
.0372	-1.4300	.8021122
.0398	-1.4000	.8533203
.0427	-1.3700	.9017227
.0457	-1.3400	.9459001
.0490	-1.3100	.9844292
.0525	-1.2800	1.0160180
.0562	-1.2500	1.0396910
.0603	-1.2200	1.0549010
.0646	-1.1900	1.0615470
.0692	-1.1600	1.0599310
.0741	-1.1300	1.0506600
.0794	-1.1000	1.0345520
.0851	-1.0700	1.0125480
.0912	-1.0400	.9856257
.0977	-1.0100	.9547504
.1047	-.9800	.9208304
.1122	-.9500	.8846943
.1202	-.9200	.8470759
.1288	-.8900	.8086106
.1380	-.8600	.7698367
.1479	-.8300	.7312019
.1585	-.8000	.6930702
.1698	-.7700	.6557311
.1820	-.7400	.6194097
.1950	-.7100	.5842757
.2089	-.6800	.5504509
.2239	-.6500	.5180185
.2399	-.6200	.4870292
.2570	-.5900	.4575066
.2754	-.5600	.4294539
.2951	-.5300	.4028572
.3162	-.5000	.3776893
.3388	-.4700	.3539138
.3631	-.4400	.3314860
.3890	-.4100	.3103565
.4169	-.3800	.2904721
.4467	-.3500	.2717777
.4786	-.3200	.2542170

TABLE 9

Fresnel field along the axis normalized to the peak aperture field E_0.

CASE # 2

TABLE 9 Continued and Concluded

.5129	-.2900	.2377334
.5495	-.2600	.2222710
.5888	-.2300	.2077748
.6310	-.2000	.1941914
.6761	-.1700	.1814687
.7244	-.1400	.1695572
.7762	-.1100	.1584087
.8318	-.0800	.1479777
.8913	-.0500	.1382205
.9550	-.0200	.1290959
1.0233	.0100	.1205646
1.0965	.0400	.1125896
1.1749	.0700	.1051358
1.2589	.1000	.0981702
1.3490	.1300	.0916617
1.4454	.1600	.0855809
1.5488	.1900	.0799005
1.6596	.2200	.0745944
1.7783	.2500	.0696386
1.9055	.2800	.0650101
2.0417	.3100	.0606877
2.1878	.3400	.0566513
2.3442	.3700	.0528823
2.5119	.4000	.0493631
2.6915	.4300	.0460773
2.8840	.4600	.0430095
3.0903	.4900	.0401454
3.3113	.5200	.0374716
3.5481	.5500	.0349754
3.8019	.5800	.0326451
4.0738	.6100	.0304698
4.3652	.6400	.0284392
4.6774	.6700	.0265437
5.0119	.7000	.0247743
5.3703	.7300	.0231227
5.7544	.7600	.0215811
6.1659	.7900	.0201421
6.6069	.8200	.0187990
7.0795	.8500	.0175454
7.5858	.8800	.0163752
8.1283	.9100	.0152831
8.7096	.9400	.0142637
9.3325	.9700	.0133123
10.0000	1.0000	.0124243

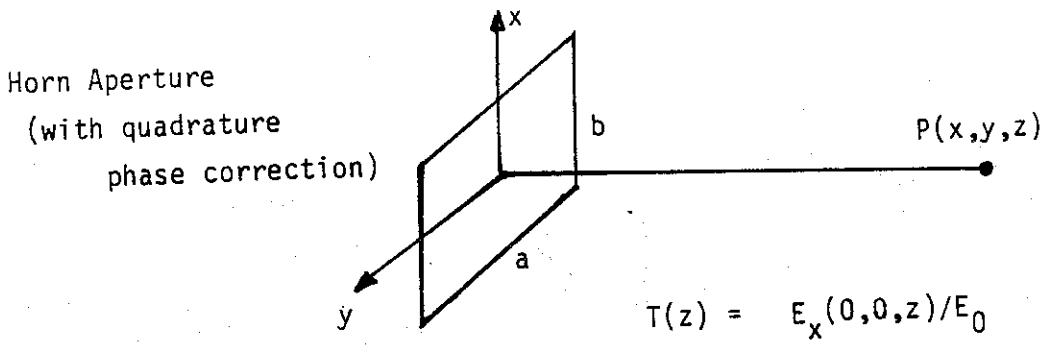

$$T(z) = E_x(0,0,z)/E_0$$

$$z_{norm} = z/ff$$

$$ff = 2(a^2 + b^2)/\lambda$$

Fresnel
a=1.433,b=1.059,lE=1.8,lH=1.972,Lamd=.3

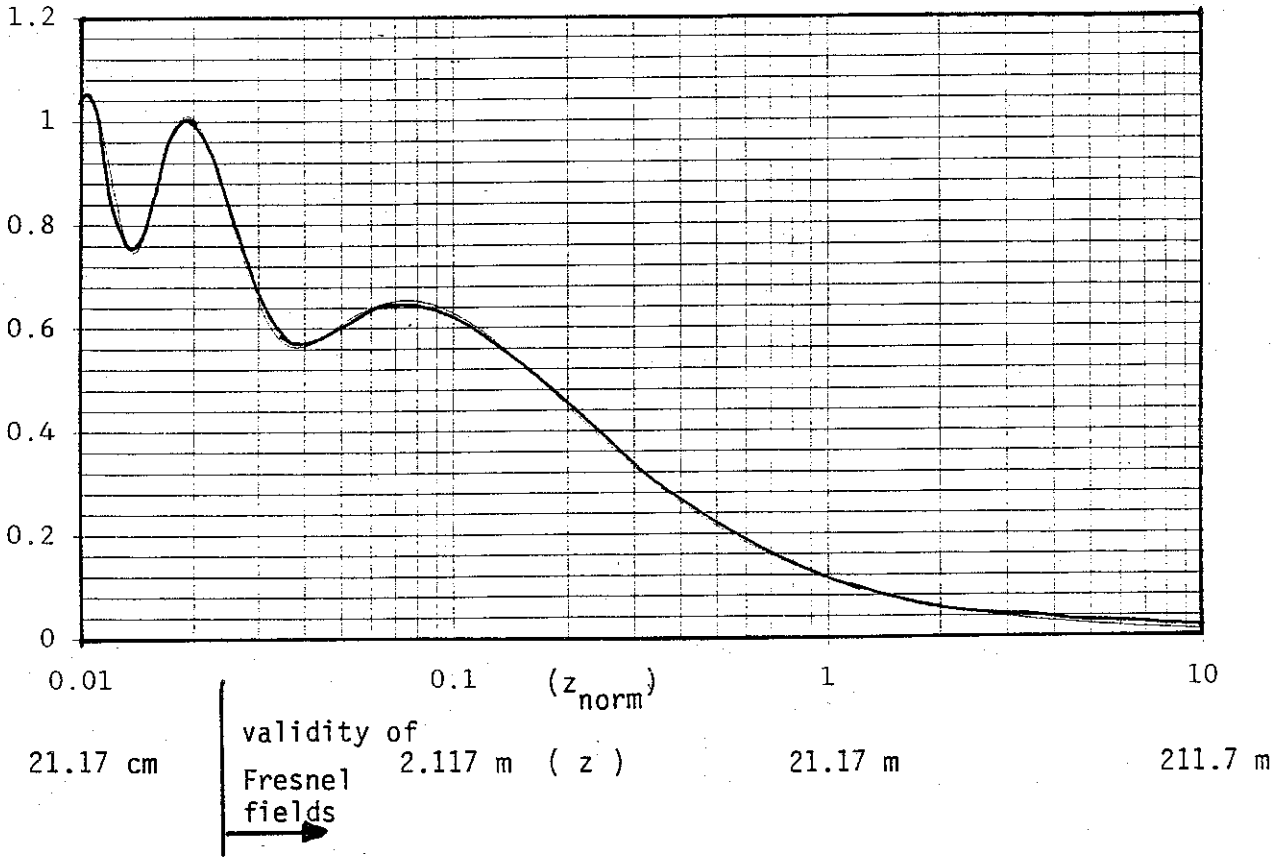

Figure 4-3. Fresnel field along the axis for Case # 1 , normalized to the peak field in the aperture

NOTE: Fresnel field formulation is valid when $z \geq (1.6\lambda)$

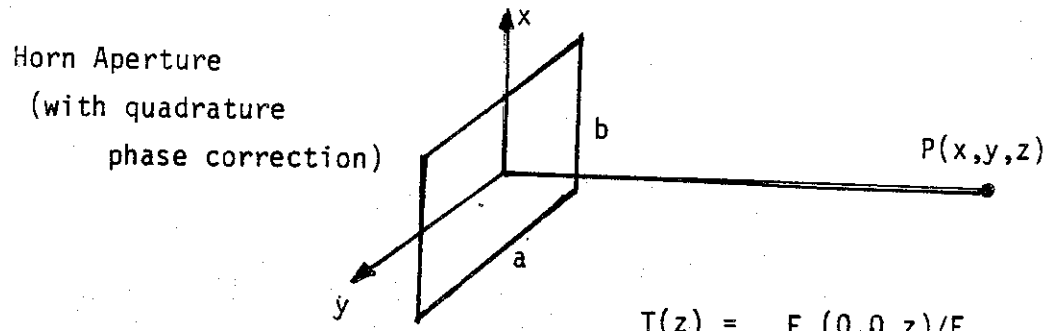

$$T(z) = E_x(0,0,z)/E_0$$

$$z_{norm} = z/ff$$

$$ff = 2(a^2 + b^2)/\lambda$$

Fresnel
a=0.6,b=0.45,1E=3,1H=3,Lamda=0.3

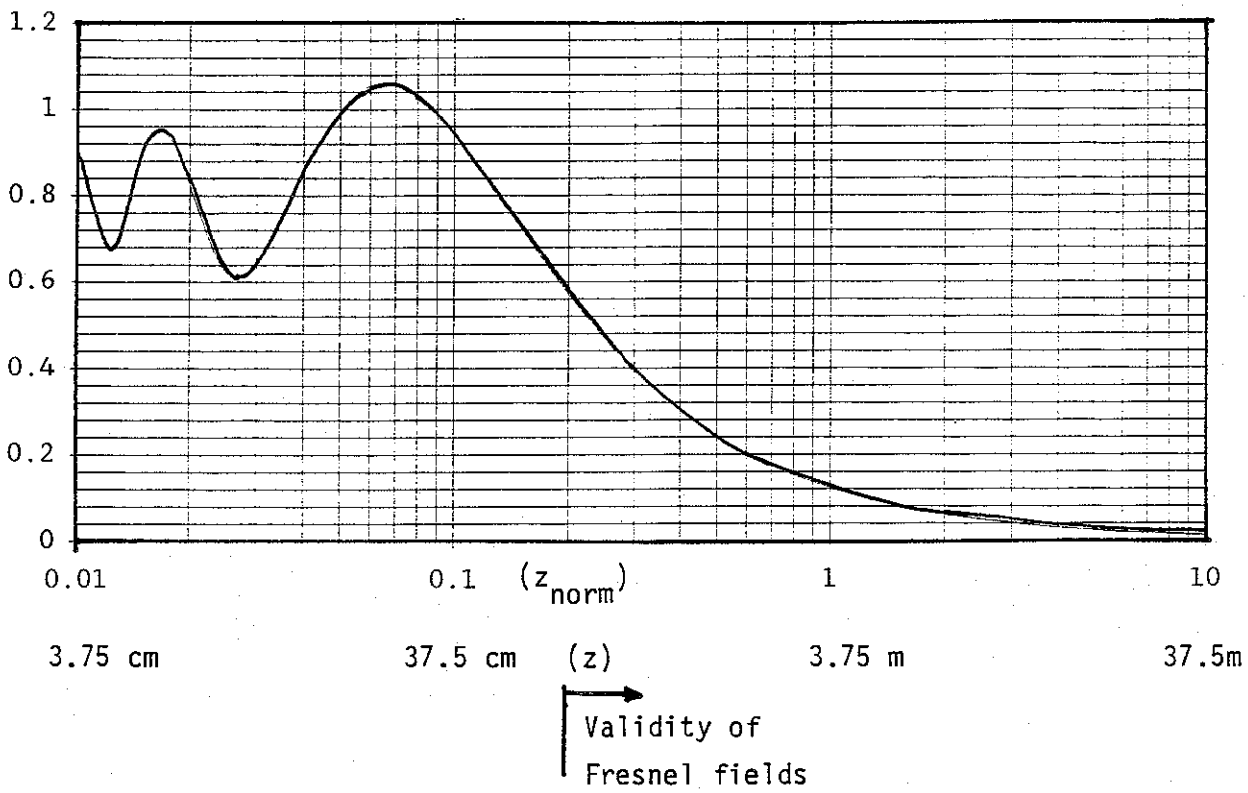

Figure 4-4. Fresnel field along the axis for Case # 2, normalized to the peak field in the aperture.

NOTE: Fresnel field formulation is valid for $z \geq (1.6\lambda)$

of the horn. This information is valuable in the design of the vacuum-air interface, which is a subject for a future report.

4.5. *Illustrative Example of Fraunhofer Fields of a Pyramidal Horn*

In this subsection we illustrate the computation of E and H plane radiation patterns of an electromagnetic pyramidal horn.

H-plane Radiation Pattern from (4.30c)

$$R_H(\theta) = \left|\frac{E_\phi}{E_0}\right| = \frac{b}{8\pi R}\,[1 + \cos(\theta)]\,\sqrt{\pi k l_H}\,F_3(\theta,\zeta_i) \tag{4.40}$$

where the pattern function $F_3(\zeta_i)$ is found in (4.31) to (4.33)

E-plane Radiation Pattern from (4.34c)

$$R_E(\theta) = \left|\frac{E_\theta}{E_0}\right| = \frac{a}{2\pi^2 R}\,[1 + cos\,(\theta)]\,\sqrt{\pi k l_E}\,F_4(\theta,\xi_i) \tag{4.41}$$

$$|F_4(\theta,\xi_i)| = \left[\left\{C(\xi_2) - C(\xi_1)\right\}^2 + \left\{S(\xi_2) - S(\xi_1)\right\}^2\right]^{1/2} \tag{4.42}$$

with

$$\xi_i = \sqrt{\frac{1}{\pi k l_E}}\left[(-1)^i\,\frac{ka}{2} - k\,\sin(\theta)\,l_E\right] \quad \text{for } i = 1, 2 \tag{4.43}$$

A computer program RADPAT is written to evaluate $R_H(\theta)$ and $R_E(\theta)$ above in their normalized form i.e.,

$$R_{NH}(\theta) = \frac{R_H(\theta)}{R_H(0)} = \frac{[1+\cos(\theta)]}{2}\left|\frac{F_3(\theta,\zeta_i)}{F_3(0,\zeta_i)}\right| \tag{4.44}$$

$$R_{NE}(\theta) = \frac{R_E(\theta)}{R_E(0)} = \frac{[1+cos\,(\theta)]}{2}\left|\frac{F_4(\theta,\xi_i)}{F_4(0,\xi_i)}\right| \tag{4.45}$$

$R_{NH}(\theta)$ and $R_{NE}(\theta)$ are computed for $0 \le \theta\ (\pi/2)$ and shown plotted in figures 4-5 and 4-6. The calculations are for the illustrative example pyramidal horns previously considered. The beam widths in the principal planes $\phi = 0$ and $\phi = (\pi/2)$ are seen to be about the same, as expected.

(see figure 4-2
for a description of the
geometrical parameters)

H-plane radiation

E-plane radiation

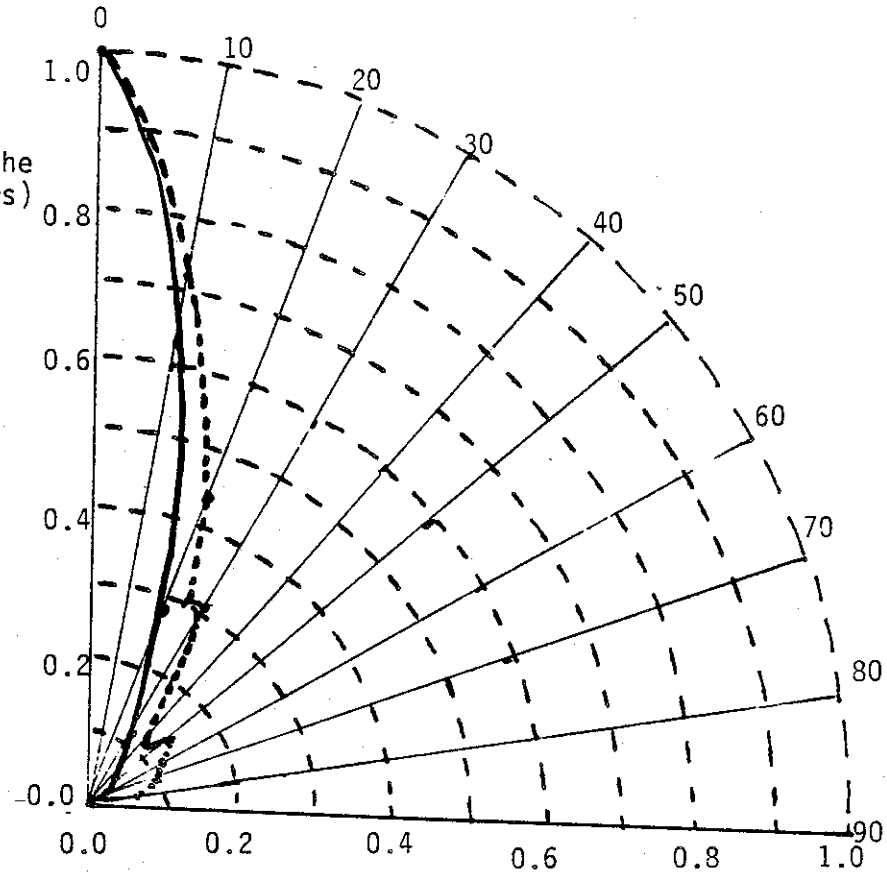

a = 1.433 m

b = 1.059 m

ℓ_E = 1.800 m

ℓ_H = 1.972 m

λ = 0.300 m

(a/λ) = 4.77

(b/λ) = 3.53 , (ℓ_E/λ) = 6 , (ℓ_H/λ) = 6.57

θ	$R_{NH}(\theta)$	$R_{NE}(\theta)$
0.	1.0000000	1.0000000
5.	.8842437	.8477986
10.	.6337972	.7170469
15.	.4253781	.6808378
20.	.2958411	.4481229
25.	.1851275	.3023182
30.	.1108546	.3079256
35.	.0831296	.1910695
40.	.0579399	.1264964
45.	.0348357	.1617869
50.	.0286330	.1260318
55.	.0262576	.0629872
60.	.0199349	.0661537
65.	.0133950	.0875000
70.	.0101438	.0870309
75.	.0096053	.0737658
80.	.0095246	.0587109
85.	.0091374	.0475199
90.	.0084874	.0414848

Figure 4-5. E and H plane radiation patterns.

(see figure 4-2
for a description of the
geometrical parameters)

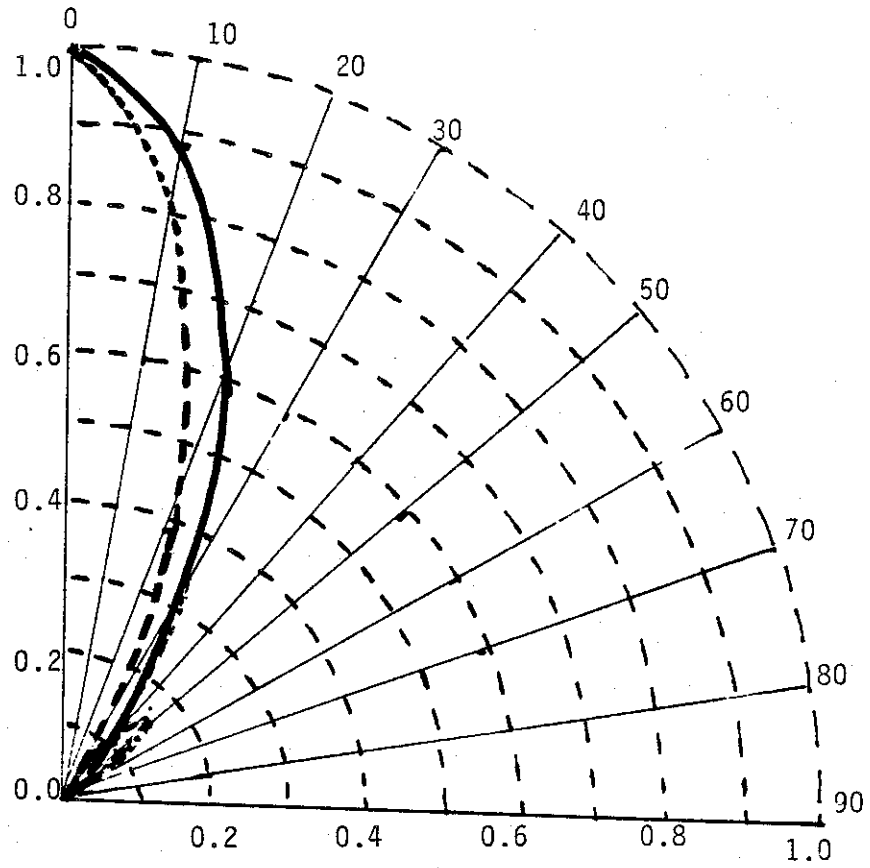

H=plane radiation

E-plane radiation

a = 0.600 m

b = 0.450 m

ℓ_E = 3.000 m

ℓ_H = 3.000 m

$(a/\lambda) = 2$

$(b/\lambda) = 1.5$, $(\ell_E/\lambda) = 10$, $(\ell_H/\lambda) = 10$

θ	$R_{NH}(\theta)$	$R_{NE}(\theta)$
0.	.9999999	1.0000000
5.	.9701276	.9490854
10.	.8853687	.8074816
15.	.7590180	.6050918
20.	.6094317	.3816798
25.	.4557624	.1776936
30.	.3141836	.0595062
35.	.1956457	.1257968
40.	.1056888	.1779629
45.	.0474686	.1897937
50.	.0314085	.1729942
55.	.0423304	.1409898
60.	.0500557	.1046050
65.	.0517764	.0709502
70.	.0497007	.0437611
75.	.0458764	.0244155
80.	.0416467	.0131243
85.	.0377361	.0089985
90.	.0344218	.0080508

Figure 4-6. E and H plane radiation patterns.

5. EM Far Fields from an Array of Pyramidal Horns

The radiation pattern of an array of identical radiators may be written as

$$\begin{bmatrix}\text{Radiated field of} \\ \text{an array}\end{bmatrix} = \begin{bmatrix}\text{Radiated field of} \\ \text{a single element}\end{bmatrix} \times \begin{bmatrix}\text{Array factor}\end{bmatrix}$$

or

$$E_a(r,\theta,\phi) = E_1(r,\theta,\phi) \times f(\theta,\phi) \tag{5.1}$$

In general, the array factor can be written as [1]

$$f(\theta,\phi) = \sum_{m=1}^{N} a_m \, e^{ju_m(\theta,\phi)} \tag{5.2}$$

with

$$u_m(\theta,\phi) = k \, \vec{r}_m \cdot \vec{1}_r \tag{5.3}$$

$$\vec{r}_m = x_m \, \vec{1}_x + y_m \, \vec{1}_y + z_m \, \vec{1}_z \tag{5.4}$$

$$\vec{1}_r = \sin(\theta)\cos(\phi)\,\vec{1}_x + \sin(\theta)\sin(\phi)\,\vec{1}_y + \cos(\theta)\,\vec{1}_z \tag{5.5}$$

where (r,θ,ϕ) is a set of spherical coordinate system and a a_m, u_m denote the amplitude and phase of the mth drive element, one of which can be a reference radiator.

It is noted that the array factor is characteristic quantity of the array, depending only on the amplitude coefficients of the N radiators and their relative positions. Array factor is independent of the type of the radiator which are arrayed together.

5.1. *Linear Array*

Consider a linear array of N elements spaced equidistantly along the z axis. Let the first element be at the origin and the spacing between any adjacent elements be d. Then the array factor is [1],

$$f(\theta) = \sum_{m=1}^{N} a_m \, e^{jkd(m-1)\cos(\theta)} \tag{5.6}$$

It is seen that the first element (m=1) at the origin serves as a phase reference. This type of an array of horn radiators is not of present interest in the HPM radiating system and is not pursued any further.

5.2. *Two Dimensional Array*

Consider a two dimensional array shown in figure 5-1 of radiating elements (e.g., pyramidal horns). The radiators are distributed in the x-y plane and a set of rectangular (x,y,z) and spherical (r,θ,ϕ) coordinates are described in the figure. The mth radiator is located by the vector

$$\vec{r}_m = x_m \vec{1}_x + y_m \vec{1}_y \tag{5.7}$$

let there be N_x, N_y radiators in each row parallel to the x and y axis respectively. We denote the equispacing along the x and y directions by d_x and d_y. Then the array factor f may be written as

$$f(\theta,\phi) = f_1(\theta,\phi)\, f_2(\theta,\phi) \tag{5.8}$$

$$f_1(\theta,\phi) = \sum_{m=1}^{N_x} a_m\, e^{jkd_x(m-1)sin(\theta)\cos(\phi)} \tag{5.9}$$

$$f_2(\theta,\phi) = b_n\, e^{jkd_y(n-1)sin(\theta)\sin(\phi)} \tag{5.10}$$

We require, in the context of HPM radiation, all of the pyramidal horns, presumably are excited by same amplitude coefficient and are in phase. Consequently, the array factor reduces to

$$f(\theta,\phi) = f_1(\theta,\phi)\, f_2(\theta,\phi) \tag{5.11}$$

with

$$f_1(\theta,\phi) = \sum_{m=1}^{N_x} e^{jkd_x(m-1)sin(\theta)\cos(\phi)} \tag{5.12}$$

$$f_2(\theta,\phi) = \sum_{n=1}^{N_y} e^{jkd_y(n-1)sin(\theta)\sin(\phi)} \tag{5.13}$$

5.3. *Circular Array of Horns*

As before, the radiated field of the array E_a is given by

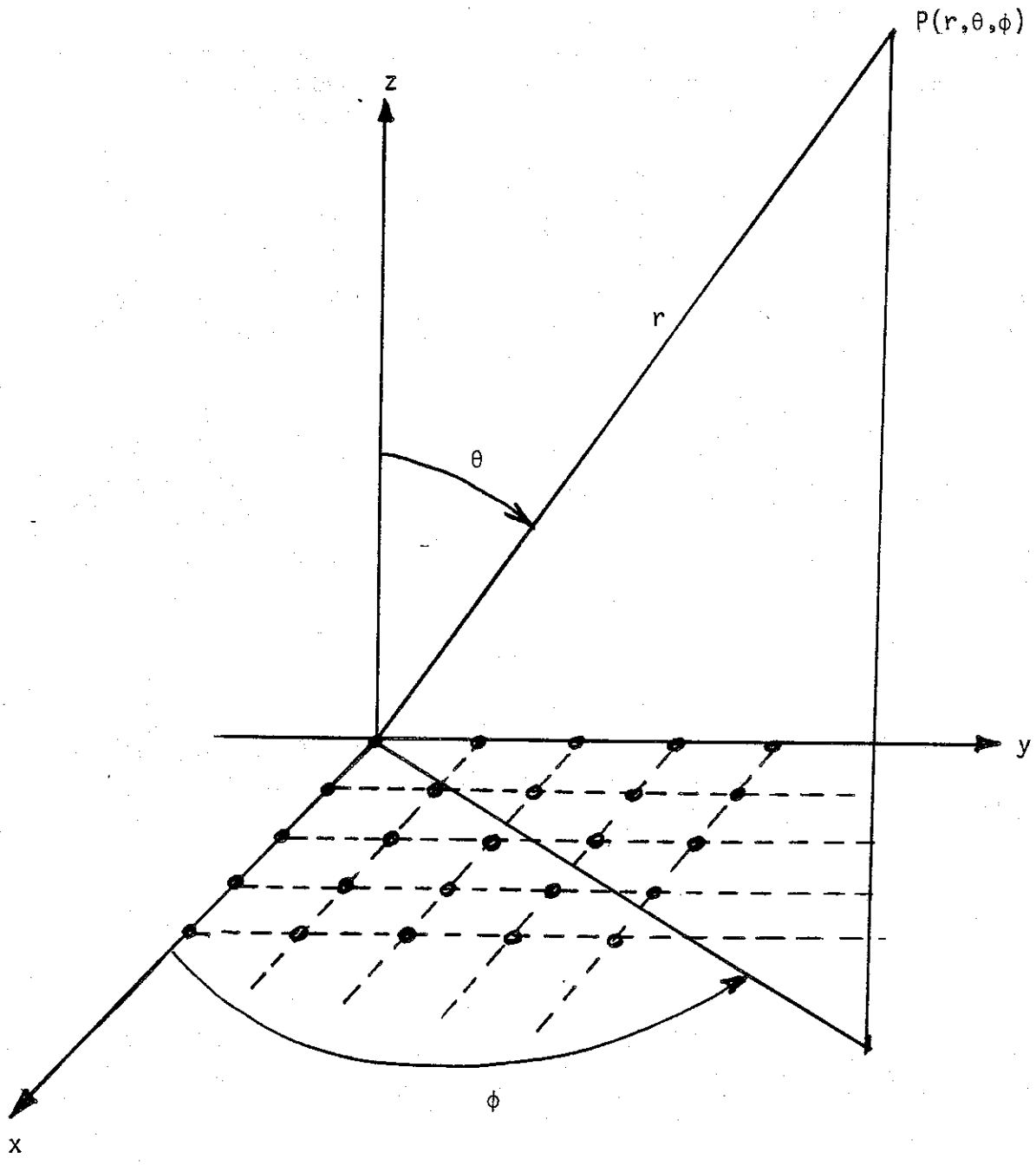

Figure 5-1. A rectangular array of radiating elements.

$$E_a(r,\theta,\phi) = E_1(r,\theta,\phi)\, f(\theta,\phi) \tag{5.14}$$

with

$$f(\theta,\phi) = \sum_{m=1}^{N} a_m\, e^{i[\delta_m + kA\, \sin(\theta)\cos(\phi-\alpha_m)]} \tag{5.15}$$

With reference to figure 5-2

$a_m \equiv$ amplitude of the mth element

$\delta_m \equiv$ phase of the mth element

$k = (2\pi/\lambda) \equiv$ wave number

$A \equiv$ radius of the circular array

Under the assumptions of identically oriented, equally spaced and fed horns, to produce a directive beam in a general direction (θ_0,ϕ_0), the individual phases have to satisfy

$$\delta_m = -kA\ sin(\theta_0)\cos(\phi_0-\alpha_m) \tag{5.16}$$

which implies, to obtain a directive beam in the direction of z-axis, i.e., $\theta_0 = 0$, we have

$$f(\theta,\phi) = \sum_{m=1}^{N} e^{j[kA\, sin(\theta)\cos(\phi-\alpha_m)]} \tag{5.17}$$

Computer programs that evaluate the electromagnetic fields from a single pyramidal horn can now be extended to include the array factor calculation.

5.4. *Horn Arrays*

We are transitioning from N evacuated waveguides via, N evacuated horns into air. The aperture surface is formed by N horns joined together either on a planar or a spherical surface. Baum [10], has considered at least 3 ways of arranging the horns on a planar surface as follows (figure 5-3)

1) in-line rectangular array of pyramidal horns
2) staggered rectangular array of pyramidal horns
3) rectangular array of rhombic or diamond shaped horn apertures.

An undesirable feature of an in-line or staggered array of horns is that the electric field distribution over the whole aperture is non-uniform. This is because when two adjacent pyramidal horns touch along the "side wall," the tangential E-field goes to zero. In other words, in the total aperture, created by such horn array, there are vertical lines, where the aperture field goes to zero.

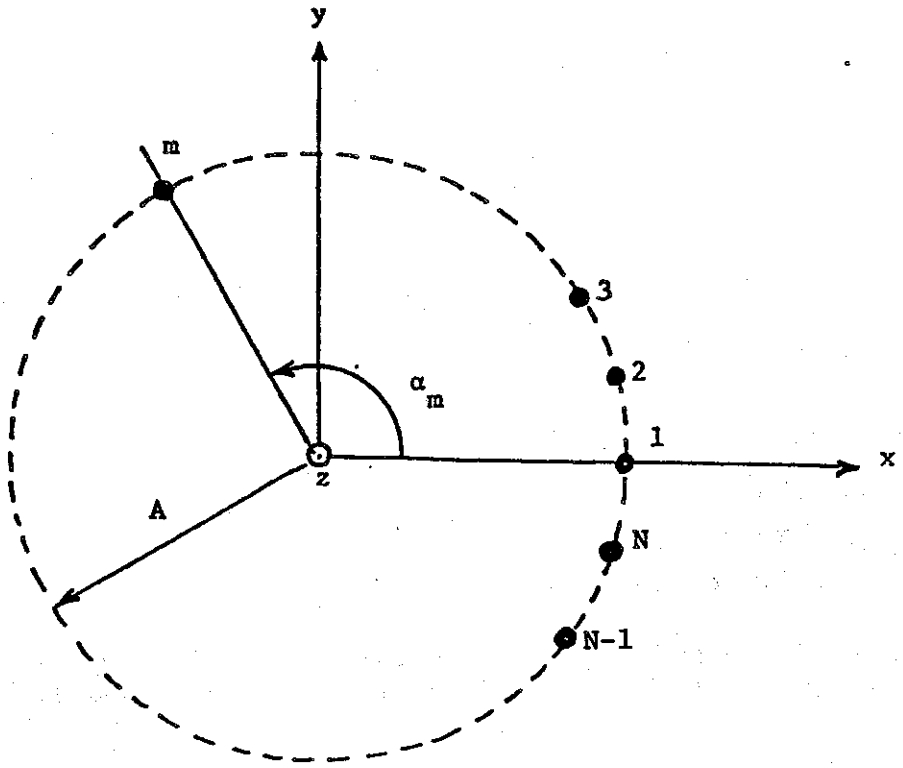

(a) Circular array of N radiating elements

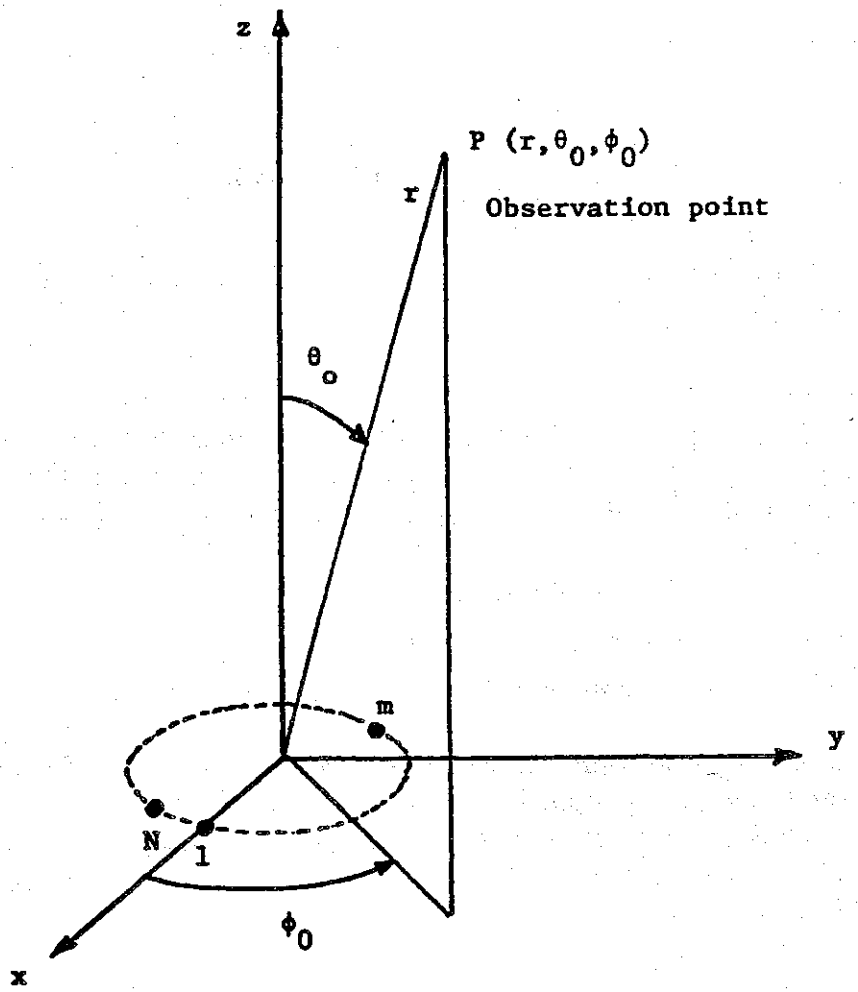

(b) Coordinate system

Figure 5-2. Geometry of a circular array.

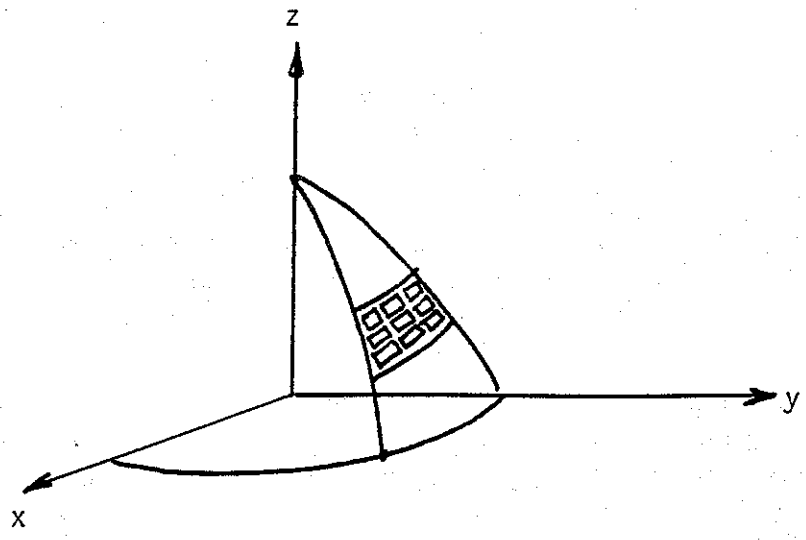

EM horns on a spherical surface

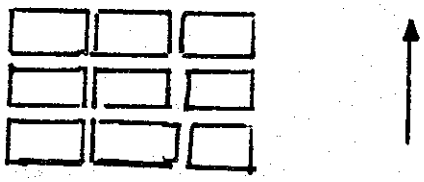

vertical stacking helps
in an in-line rectangular
array

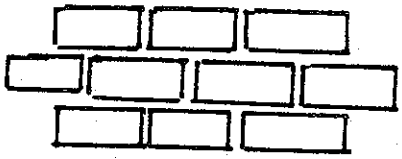

horizontal packing creates
non-uniform aperture fields
staggering the array should help

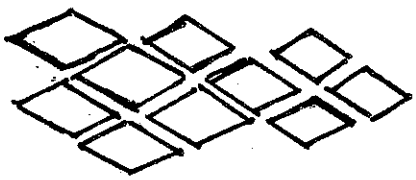

diagonal or rhombic horn array

Figure 5-3. Different horn array arrangements.

In array 3 listed above, the non uniformity of aperture field is considerably reduced. An element of the diagonal horn array is shown in figure 5-4. Diagonal horns [15] have been considered in the past where all cross sections through the horn including the aperture are square. However, if we used rhombic shaped aperture with width to height ratios of about 2, the dominant mode of propagation is still $H_{0,1}$. If the aperture indicated in figure 5-4 is arrayed in two dimensions, one could observe that the aperture field is significantly more uniform than, in an array of rectangular apertures.

Yet another variation on the rhombic horn is to round off the edges of the rhombus. As long as the horizontal dimension in larger than the vertical dimension $H_{0,1}$ like mode of propagation exists. The actual arrangement of horns on a planar or spherical surface is best left to a detailed experimental study with low power microwaves (LPM) from commercially available magnetron sources for example. The array of horns illustrated in figure 5-3 and possibly other arrays can be considered in an experimental LPM study.

With regards to the dielectric interface for the horn array, once again Fresnel field computation similar to those in the previous Section 4 can be performed for the array to determine the location of the interface.

A practical arrangement would be to have a vacuum-SF_6 interface in the waveguide, so that a portion of the waveguide and the horn(s) contain SF_6 at 1 atmospheric pressure. A polyethelene bag containing 1 atmospheric pressure of SF_6 then occupies a volume between evacuated waveguide and the outside environment. This volume is large enough so that the fields on the outside surface of the bag are acceptably below the air breakdown values. Since the evacuated waveguide holds off the electric field without breakdown, SF_6 at 1 atmospheric pressure should be adequate as a transition medium between vacuum and air. One could avoid the pressurization of SF_6 with this scheme. The actual breakdown field at sea-level and other altitudes is a function of pulse width and frequency and available results concerning the breakdown should be used in the design of the interfaces.

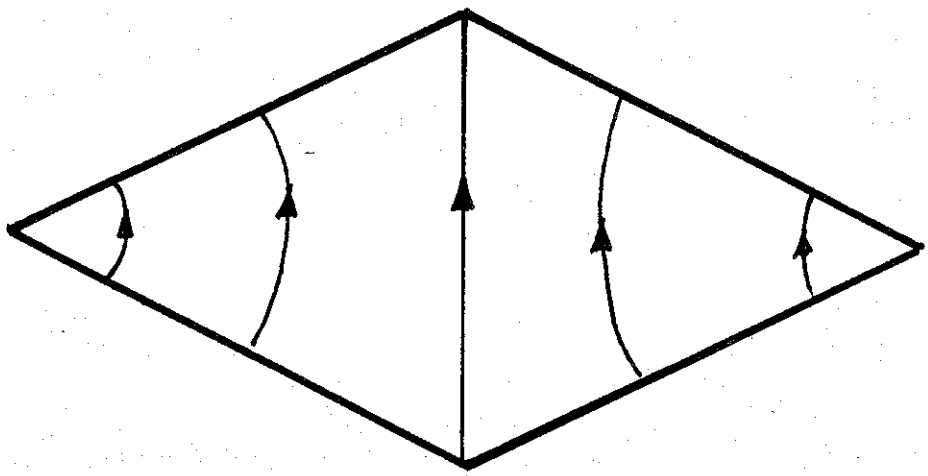

Figure 5-4. Rhombic or a diagonal horn aperture with the princial electric fields.

6. A Brief Review of HPM Sources

Microwave generation can be accomplished in many ways, and as a result many varieties of sources have been developed. At high power levels (above 100 MW) also, several types of sources exist, such as magnetrons, klystrons, gyrotrons, vircators, free-electron lasers (FELs) and beam-plasma devices [16 to 21].

Recall that, our present interest is in the frequency range below 3GHz. For this reason, we have surveyed available sources in the somewhat broader range of 1 to 10 GHz. There are several ways of classifying microwave sources, but they all seem to have some essential features. For example, in nearly all of the sources, the kinetic energy of the electrons (charged particle) in a beam is converted into microwave energy (wave). Consequently, wave-particle interaction is the basic physical mechanism for HPM generation.

In [22], one categorization of the HPM sources, based on wave-particle interaction concepts has led to the following.

1) Parametric Devices	-	a) Ubitrons
2) Plasma Devices	-	a) Virtual cathode oscillators (VIRCATORs), b) Beam-Plasma Interation and c) Orbitrons
3) Fast Wave Devices	-	a)Cyclotron resonant masers (CRMs) such as gyrotrons and cyclotron autoresonant masers (CARMs)
4) Slow Wave Devices	-	a) Magnetrons, b) Backward Wave Oscillators (BWOs), c) Cerenkov masers

Some basic concepts of HPM generation are reviewed here. It is also noted that in all of the devices, one has the following ingredients: a) power supply, b) pulse generator, c) electron beam generator, d) a wave-particle interaction region in which the HPM is generated and e) an extraction element by which HPM is put out. Such a breakdown of a generic HPM source is illustrated in figure 6-1.

In the above classification of devices, fast and slow waves are distinguished as follows. In fast wave devices, the phase velocity of the electron-beam is greater than speed of light, whereas in a slow wave device, the wave-particle interaction is extended in time by providing a slow-wave RF structure. Examples in later sections will further clarify this distinction.

6.1. *Underlying Physical Principles of HPM Sources*

HPM sources are transient generators that produce a short burst of energy, lasting for times of the order of a microsecond or less. As noted earlier, they are driven by a transient high-voltage pulse. In the nuclear electromagnetic pulse (NEMP) simulation such pulses (rise times of the order of 5 ns and variable decay time) are routinely developed, and have been adapted as drivers for a HPM source. A good example of such a merger of technologies is a Marx pulser driving a relativistic magnetron. The

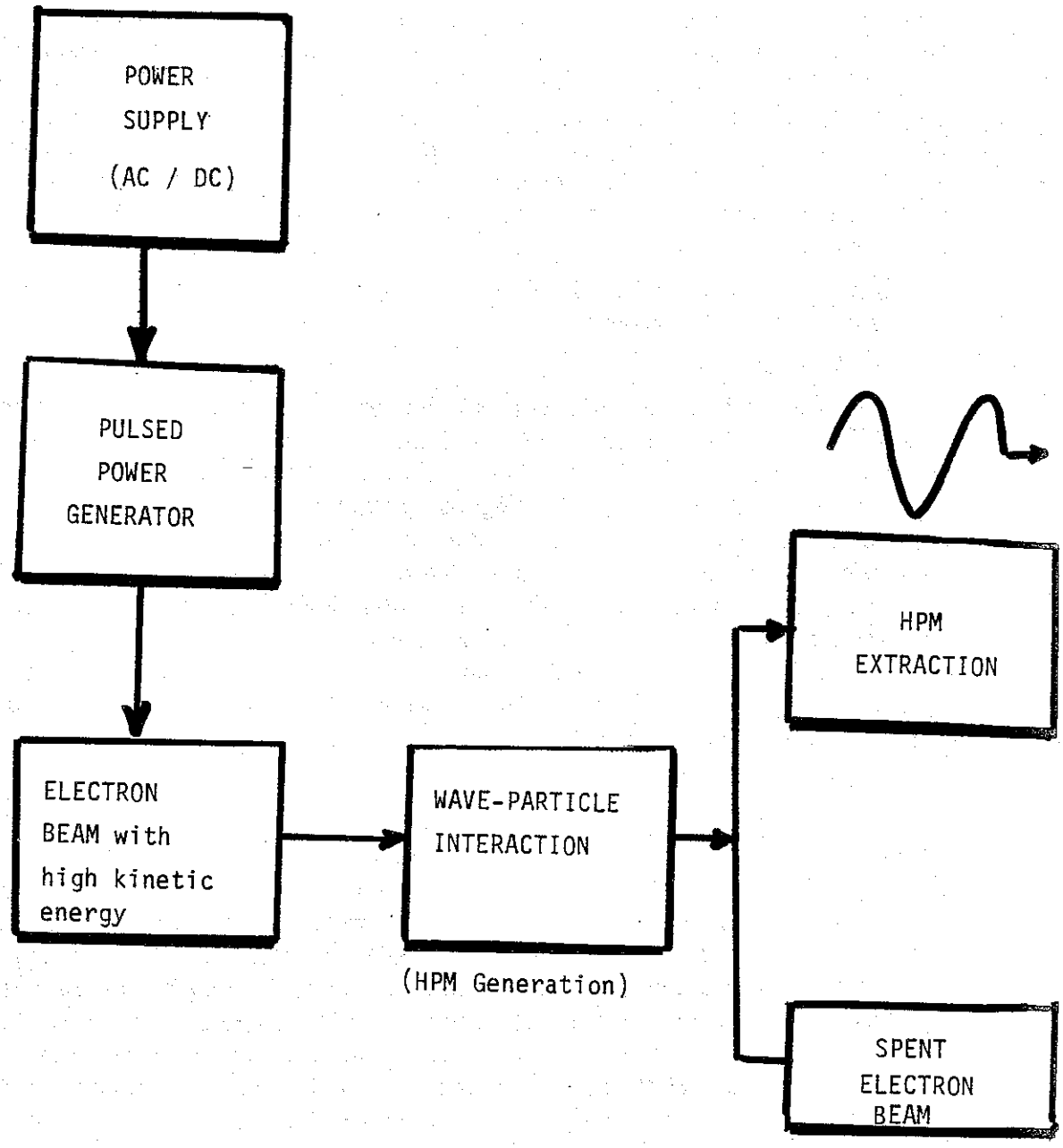

Figure 6-1. Essential ingredients of a HPM source

high-voltage Marx pulse is applied to th anode block in the magnetron relative to the cathode for the production and injection of intense electron beam into the wave-particle interaction region. Such electrical pulses required for e-beam production are available commercially up to a power level of 1 TW = 10^{12} W. Even with a device that is 10% efficient in converting this pulsed electric energy into microwave energy, 100 GW of microwave power appears feasible. Of course, there are many complex engineering or technological problems in attaining such high levels of HPM in a single source. With the present state of the art, power levels are limited to less than 10 GW of HPM in the 1 to 10 GHz frequency regime. As one moves up in frequency above 10 GHz, the power levels attained drop significantly, as seen in the following section, which reviews such data.

Returning to the subject of physical principles, we consider the four types of devices listed in the previous section.

6.1.a. Ubitrons

The theory of ubitron operation is quite simple, consisting of free electrons (i.e., unbound or free from nuclei) which oscillate transversely, due to the presence of a periodic magnetic field. The oscillating electrons radiate. The combination of this radiated field and the "wiggler" magnetic field tends to bunch the electrons in the axial direction (figure 6-2) thereby coherently building up the emitted radiation. There are basically two physical regimes for ubitrons, called the low energy (1-2 MeV) regime and the high energy electron beam (10-10,000 MeV) regime. The merits and disadvantages of both of these regimes have been extensively studied in theory and in experimental studies at Naval Research Labs (NRL), Lawrence Livermore National Labs (LLNL), Stanford University and other research organizations. The output frequency from ubitrons is typically above 30 GHz and is not of present interest.

6.1.b. VIRCATORS

It has been well known that when the limiting current of a diode is exceeded, a virtual cathode is developed. With reference to figure 6-3, a field emitting cathode generates an electron beam which passes through an anode. If the electron beam current exceeds the space charge limiting current, a virtual cathode is developed beyond the anode. The virtual cathode then repels or turns some of the electrons back into the anode, by creating a potential well. The reflected electrons are reflected in turn from the cathode. There is no magnetic field in the device and the reflexing electrons make a few transits between the real and virtual cathode, before being lost to the walls. The reflexing electrons, then radiate a coherent microwave energy in the axial direction, at a frequency roughly given by c/(2d) or a wavelength λ = 2d, i.e., half wavelength of resonance is the anode to cathode distance. The chief advantage of VIRCATORs is their inherent ability for tuning the output frequency, by varying the anode-cathode gap (d). An example of this tunability is shown in figure 6-4 from [20].

The output from the VIRCATOR is typically extracted into a cylindrical waveguide, downstream from the diode. This results in a transverse magnetic propagation or E-mode in the cylindrical waveguide. Other choices are i) transitioning from a cylindrical to a rectangular guide with $H_{0,1}$ mode in the axial direction or ii) radial extraction directly into rectangular waveguides. The second scheme of radial

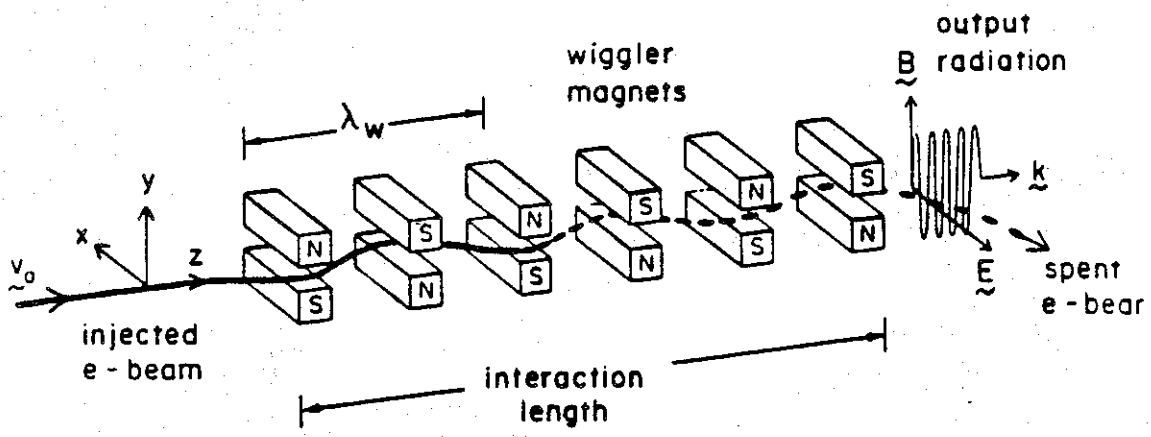

Figure 6-2. Schematic diagram of a typical ubitron (also called an FEL) configuration.

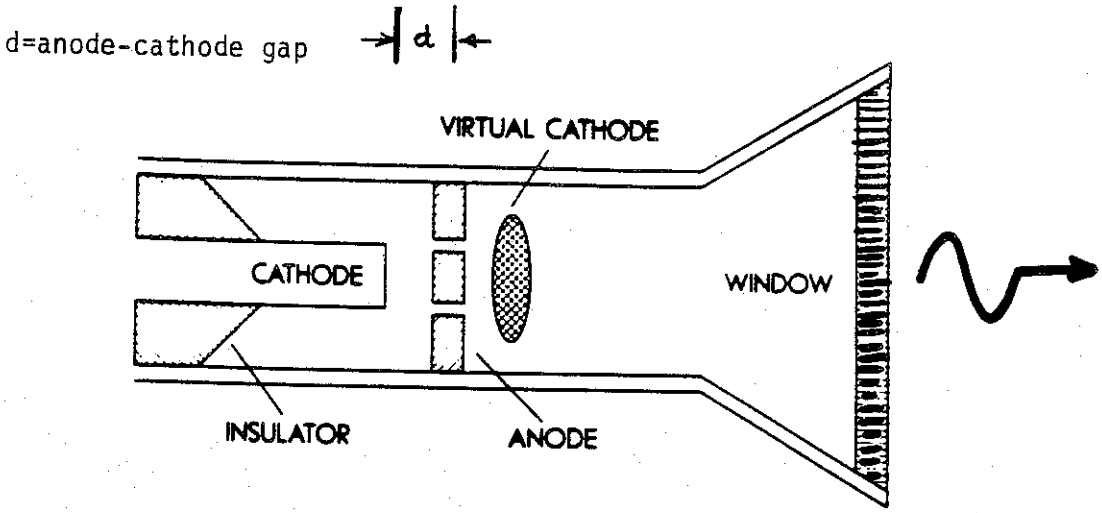

Figure 6-3. Conceptual sketch of a VIRCATOR

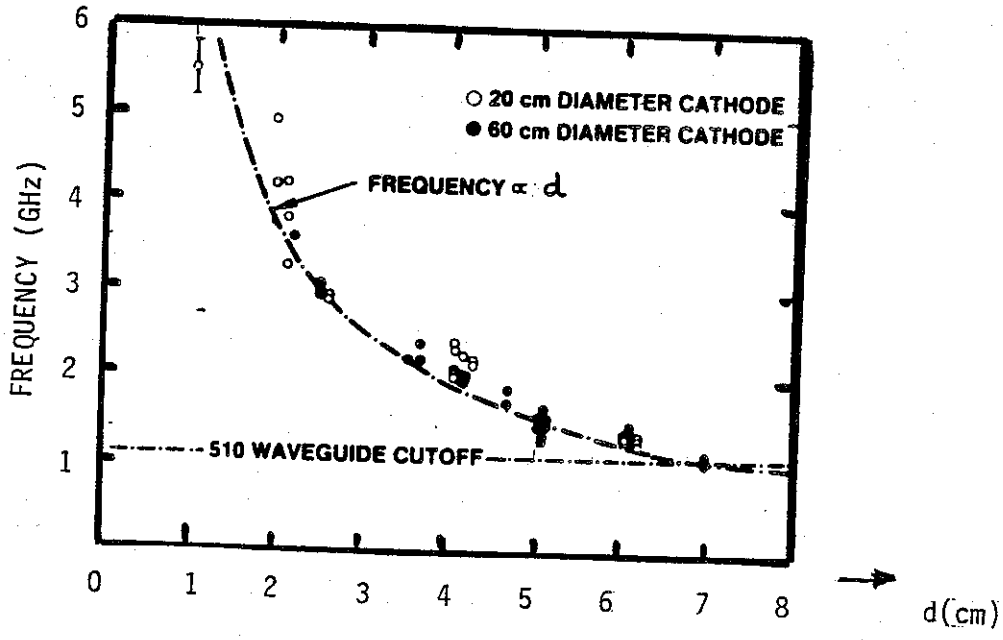

Figure 6-4. Tuning ability of a VIRCATOR (Ref. [20])

NOTE: VIRCATORs have been developed to generate HPM levels of 1 to 10 GW in the frequency range of 1 - 6 GHz.

extraction into rectangular waveguide operating in the fundamental $H_{0,1}$ mode has also been done [20].

6.1.c. Gyrotron (fast wave device)

A gyrotron, schematically shown in figure 6-5 is a HPM tube that emits coherent radiation at the electron-cyclotron frequency or its harmonics. Basically, the electrons follow helical paths around the lines of externally applied magnetic field, in the presence of an electromagnetic wave. The externally applied magnetic field and the electric field in the electromagnetic wave are orthogonal to each other. When the electrons become bunched in phase with their cyclotron orbits, there will be a net flow of energy from the electron beam to the electromagnetic wave. The electron cyclotron frequency is directly proportional to the axial magnetic field and inversely proportional to the total electron energy. These two quantities, i.e., magnetic field and e-beam energy are adjusted for phase bunching and coherent radiation of HPM.

6.1.d. Magnetrons (slow wave devices)

Many types of cross-field devices exist at low power levels in microwave generation. However, of these various types, a magnetron device has been extrapolated to HPM generation, in its relativistic form. A relativistic magnetron is distinguished from a conventional magnetron in the following sense. The electron beam generation in a conventional (low power level) magnetron is by thermionic and secondary emission processes, while in a relativistic magnetron, the electron beam generation is by a field emission process owing to the high field levels. The relativistic magnetron configuration is shown in figures 6-6 to 6-8. It employs the A-6 cavity developed originally at M.I.T. [24,25]. The output is extracted in 6 rectangular waveguides in this S-band relativistic magnetron and a cross sectional view of these 6 rectangular waveguides is indicated in figure 6-9. The polarization of the electric field in these 6 waveguides indicate the need for phase shifters that can operate at these high-power levels. The cross sectional view, after phase shifting is shown in figure 6-10. The six evacuated waveguides can lead into the feed system, which is a part of the overall radiating system for the HPM. The frequency of operation of the device shown in these figures is 2.8 GHz.

Table 10 lists a comparison of conventional and relativistic magnetron parameters. The fundamental difference between these is the nature of electron beam generation as noted already. Also, observe that the voltage applied to anode block relative to the cathode is of the order of a few MV and the current is in the range of 10's of KA, which means the dc power into the device is 10 GW or higher. The efficiency of such a device is typically in the range of 30% or less. Magnetrons are inherently unstable if operated at efficiencies significantly above 30%.

Table 11 lists operating levels of several relativistic magnetrons developed in the U.S. and U.S.S.R. This table is reproduced here from [22] (1987). It is observed that the frequency ranges from 2.4 to 9.2 GHz and the power level is 3 GW or less. Recently, relativistic magnetrons are also being developed in the industry at a lower frequency of 1 GHz.

In this section, we have reviewed the basic physical phenomenon of each class of

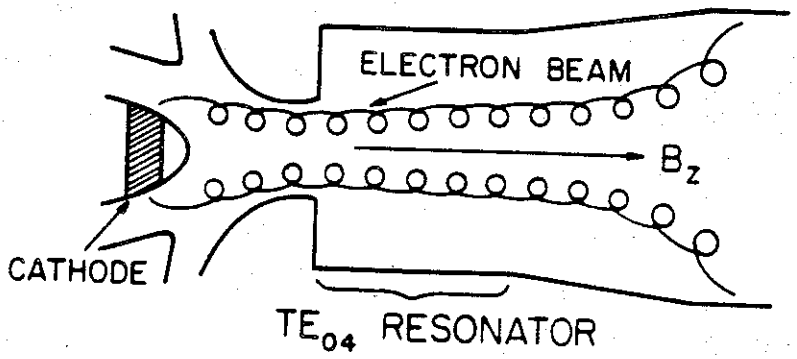

a) Simple Gyromonotron

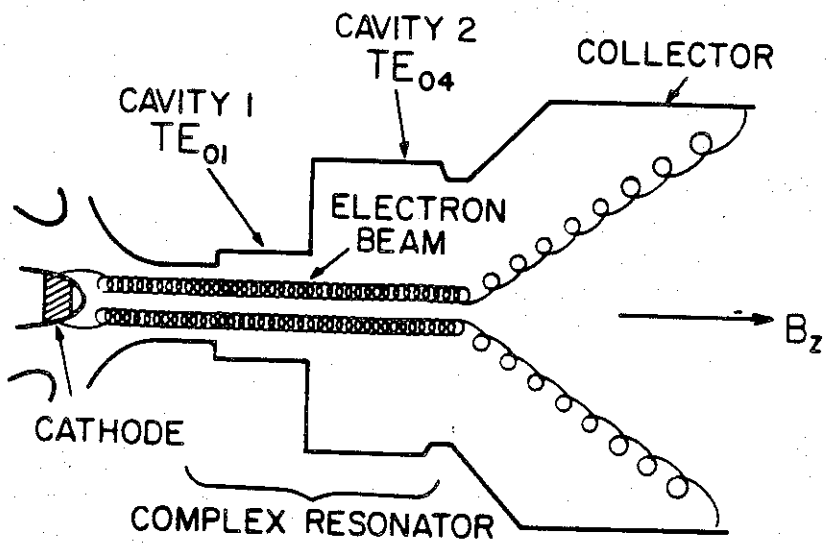

b) Coupled Cavity Gyrotron Oscillators

Figure 6-5. Gyrotron configurations [23].

NOTE: Gyrotrons have been developed in the frequency range of 3 to 100 GHz producing power levels of 1 GW at 3 GHz and about 10 MW at 100 GHz.

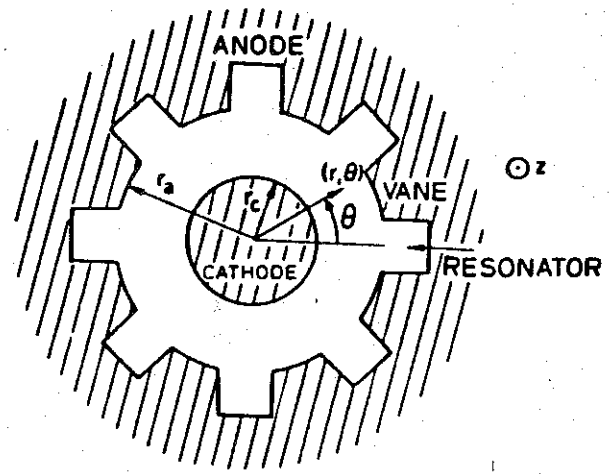

NOTE:
Figures 6-6 to 6-8
Tables 9 and 10 are from
Chapter 10 by J. Benford [22].

Figure 6-6. Geometry of a coaxial magnetron

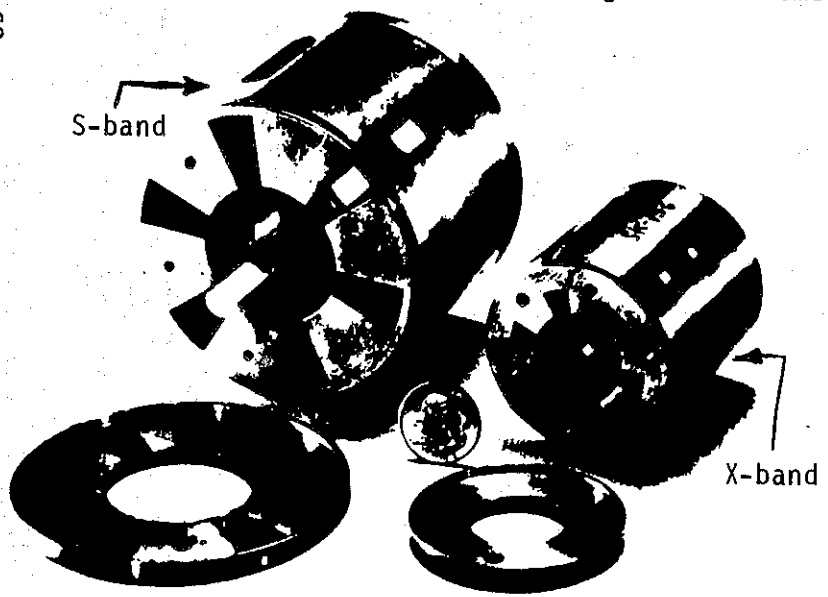

Figure 6-7. A-6 cavity (anode blocks) for S and X band magnetrons

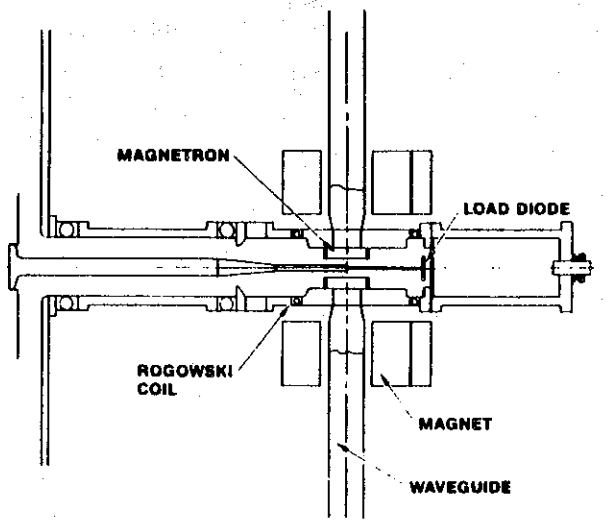

Figure 6-8. S-band relativistic magnetron with 6 extracting waveguides

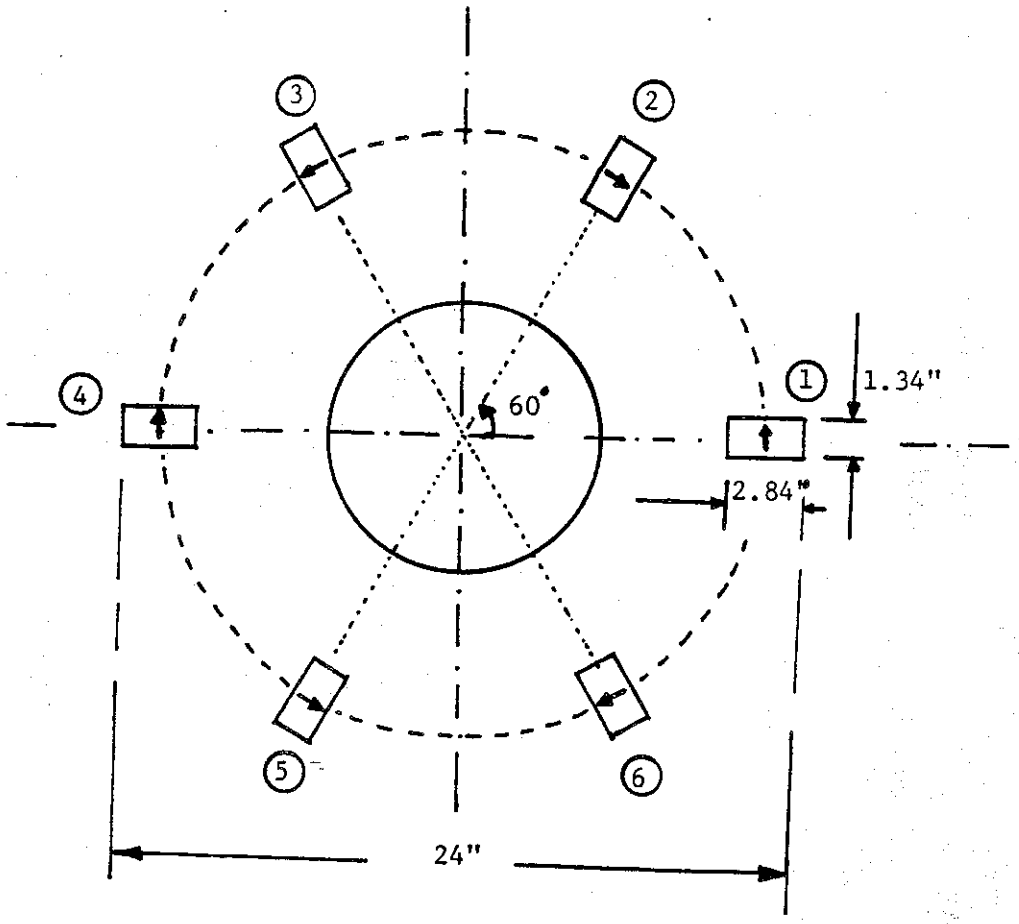

Figure 6-9. The end view of 6 waveguide extractions with dimensions and relative phases (adjacent ones are out of phase by 180 degrees)

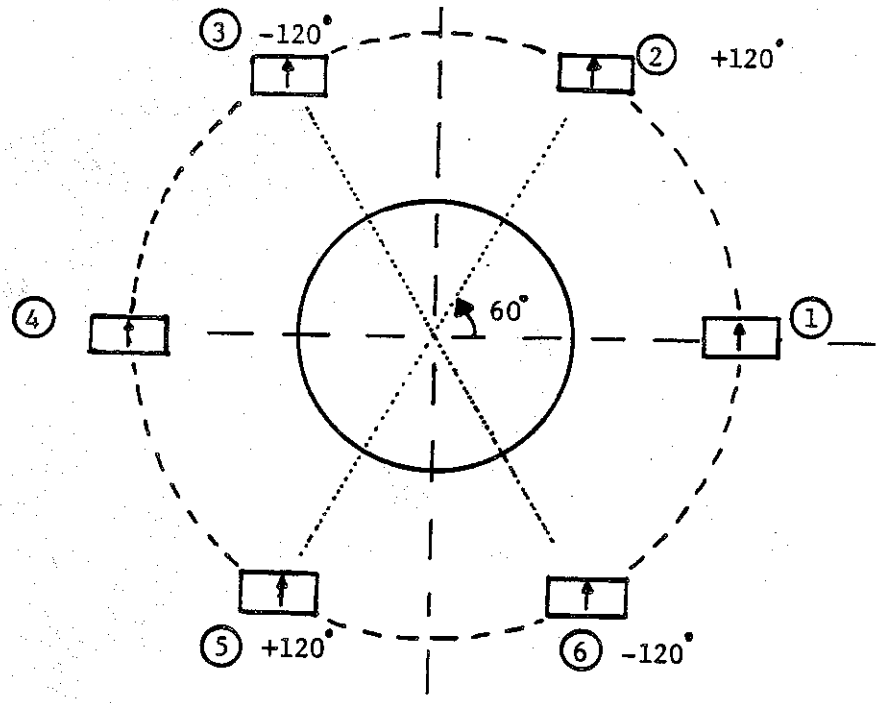

Figure 6-10. The end view of waveguides after phase adjustments as indicated

PARAMETER	CONVENTIONAL	RELATIVISTIC
Voltage	≤100 kV	~1 MV
Cathode	Thermionic and secondary emission	Field emission
Current	~100 A	≥10 kA
Pulse duration	≥1 μs	≤100 ns
Risetime	≤ 200 kV/μs	~100 kV/ns
Power	≤10 MW	≥1 GW
Efficiency	~50%	≤30%

TABLE 10 Comparison of conventional (LPM) and relativistic (HPM) magnetron parameters

Laboratory	*Parameters*													
	f (GHz)	V (MV)	I (kA)	B (T)	P (GW)	Δt (ns)	E (J)	η (%)	N	$\sigma = r_c/r_a$	r_a (cm)	h (cm)	*Mode*
MIT[a] A6	4.6	0.8	14	1.0	0.5	30	15	4	6	0.75	2.1	7.2	2π
MIT M8	3.7	1.7	4	0.46	0.4	30	12	12	8	1.47	2.9	5.1	π
MIT M10	3.7	1.6	9	0.7	0.5	30	15	3	10	1.22	3.8	4.6	π
LLNL[b]	3.9	0.9	16	1.6	4.5	16	72	30	6	0.75	2.1	7.2	2π
SRINP[c] #1	2.4	1.1	4	1.2	2.0	50	100	45	6	—	—	—	π
SRINP #2	2.4	0.45	6	0.4	0.8	300	240	30	6	—	—	—	π
NRL[d]	3.2	0.6	5	0.2	0.8	30	24	27	54	1.10	19.4	5.1	π
Stanford[e]	3.3	0.42	3	0.15	0.02	40	1	2	12	0.50	5.1	9.5	π
IAP[f] #1	9.1	0.6	7	0.6	0.5	20	10	12	8	—	—	—	π
IAP #2	9.2	0.95	40	1.0	4.0	15	60	11	8	—	—	6.5	π
Sandia[g]	3.1	1.0	10	0.3	0.25	50	12	3	12	1.3	5.22	9.23	π
PI[h]	2.8	0.7	20	1.0	3.0	20	60	20	6	0.6	2.1	7	π
PI[h]	8.3	1.0	30	1.0	0.3	10	3	0.2	6	0.48	1.4	6	π

[a] Massachusetts Institute of Technology
[b] Lawrence Livermore National Laboratory
[c] Scientific-Research Institute of Nuclear Physics, Tomsk, USSR
[d] Naval Research Laboratories
[e] Stanford University
[f] Institute of Applied Physics, Gorki, USSR
[g] Sandia National Laboratory
[h] Physics International Company

TABLE 11. Summary of relativistic magnetron parameters.

The above tables are reproduced here from [22].

devices via illustrative examples. We now proceed in the following to present the output power levels from various devices as a function of frequency.

6.2. *Experimental Data on HPM Sources*

In the previous subsection, we briefly reviewed various types of high-power RF sources. There is a vast amount of experimental studies on these devices at various governmental laboratories, universities and industries in the U.S. and elsewhere. Open-literature papers are continuously published, the latest being reference [18], dealing with various aspects of this emerging technology.

Florig [19] published in 1988, a summary of experimental data dealing with the peak power attained in high-power RF sources as a function of frequency in the U.S. and U.S.S.R. The power levels ranged from 1 MW to 20 GW, while the frequency ranged from 1 to 200 GHz. The key feature that emerges is almost a monotonic decrease in power levels with increase in frequency. Swegle [21] has updated Florig's data in his recent (May 1990) publication. Swegle's [21] finding is presented here in figure 6-11 with a minor addition.

A review of available sources and experimental data leads one to make the following observations:

1. High-power sources are being developed as laboratory experiments, not necessarily geared for specific engineering applications.
2. Large electric pulses driving conventional microwave sources have yielded HPM levels (above 100 MW)
3. The pulse duration of HPM radiation is typically in the range of hundreds of nanoseconds, resulting in energy content of upto 600 Joules.
4. In the 1 to 10 GHz range, VIRCATORs, Relativistic Magnetrons and Reflex Klystrons have proved successful. This is the frequency range of interest for the present.
5. In the 10 to 50 GHz range, BWO and TWT have been successfully developed.
6. Also at frequencies above 35 GHz, ubitrons are available.

It is also noted that there is inadequate attention focused on the extraction of HPM from the source. One reason for this may be that these sources are developed by high-voltage and plasma physics researchers and conventional microwave or electromagnetic researchers are not playing a significant role in the source development.

Recalling that our present interest is in the 1 to 3 GHz frequency regime, relativistic magnetrons, klystrons and VIRCATORs, it is emphasized that these devices presently are capable of delivering HPM levels of 1 to 10 GW.

6.3. *General Remarks on HPM Sources*

It is observed that in the frequency range of 1 to 10 GHz, relativistic magnetrons, klystrons and VIRCATORs provide HPM signals extracted in circular or more typically in rectangular waveguides. The available power levels are in the range of 1 to

Addendum: A 400 Joule, 100 to 150 ns pulse generation has been reported [27] on Aurora facility. This translates to a power level of 2.6 to 4 GW at frequencies below 1 GHz.

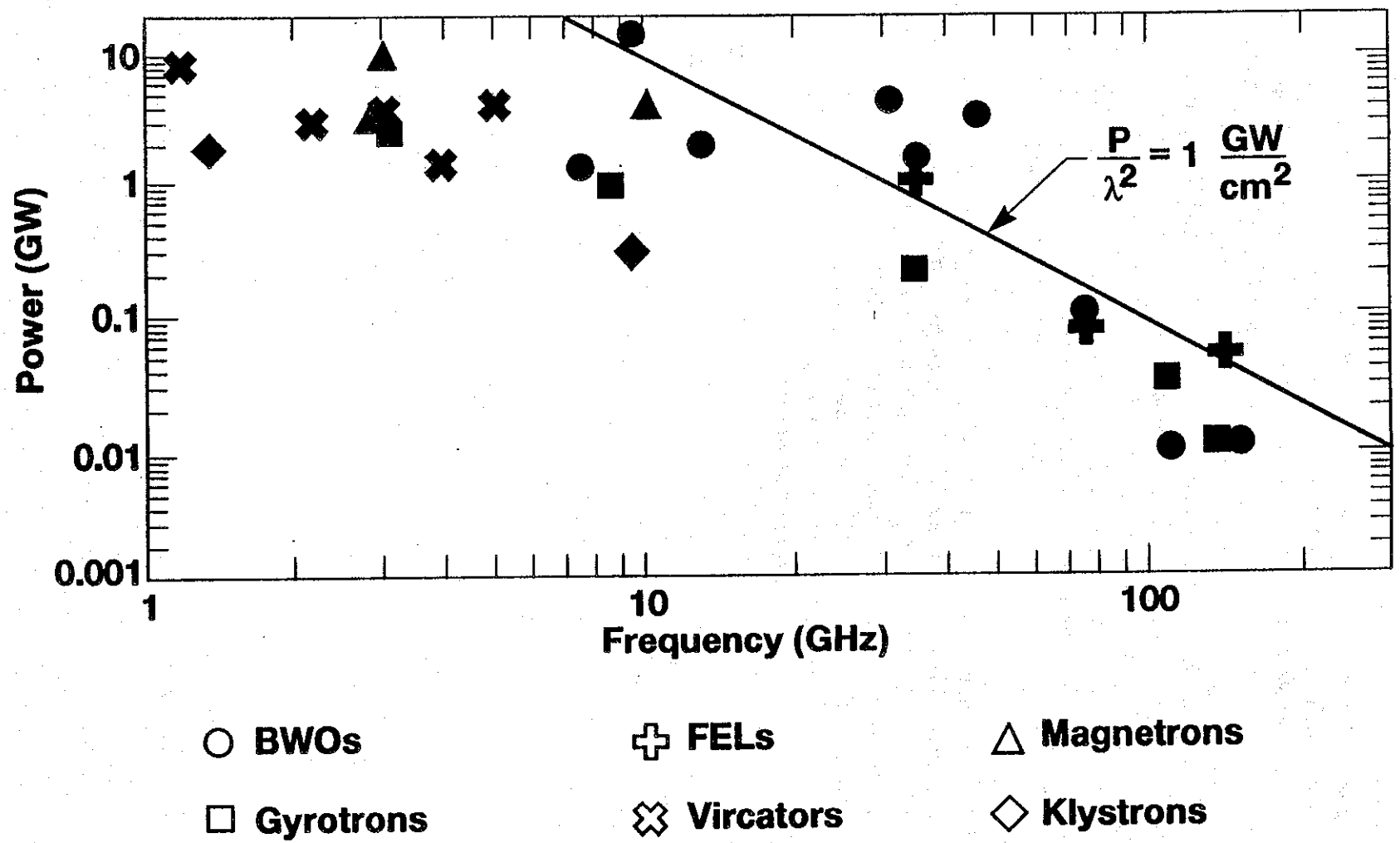

Figure 6-11. Summary of experimental data on high-power RF sources [21].

10 GW as can be seen in figure 6-11.

It is emphasized that extracting the HPM signals by rectangular waveguides is both classical and efficient. The design of the power extraction circuit should be such that the rectangular waveguide is excited in its dominant $H_{0,1}$ mode of propagation and the frequency is slightly below the next higher mode in the interest of maximum power handling capability. If power levels of over 10 GW is required there are some inherent limitations in a single device, such as the maximum sustainable electric field levels in resonant cavities for a given size. So Benford et al., [28] have proposed and are developing, phase locked oscillator groups. Baum [29] has proposed using C_N symmetry group arrangement for phase locking oscillator groups. In practice, phase locking of relativistic magnetrons has been achieved at power levels of about 3 GW at a frequency of 2.8 GHz. Extensions to 10-100 GW appears feaxible [29] with groups of oscillators.

We conclude this note by noting that it is efficient to design the source so that the HPM signals are available in N (greater than or equal to 1, depending on the power level, frequency etc.) rectangular waveguides which are evacuated to sustain the electric field levels. HPM sources which meet this criteria, albeit not all waveguide outputs in phase, are already available. The evacuated waveguides carry HPM in the single dominant mode of propagation, while avoiding overmoding problems. It is not efficient to extract the power in a overmoded waveguide and then include modal filters downstream.

7. Summary

We have considered various aspects of a radiating system for high power microwave beams. This note has considered various classical radiating systems and their applicability for HPM radiation. It is concluded that reflector antennas in general and an offset Cassegrain System in particular are well suited for generating directive HPM beams. An efficient feed system consists of rectangular waveguides and pyramidal horns. Power handling capacity of rectangular waveguides and the near and far fields from pyramidal horns are also discussed with illustrative examples for 1 GHz and 3 GHz systems. In addition, array factors for two-dimensional arrays of radiating elements are discussed. A brief review of HPM surces is also included. It is anticipated that future notes will consider more complete design and performance considerations of HPM radiating systems.

References

[1] *Antenna Theory, Parts 1 and 2*, edited by R. E. Collin and F. J. Zucker, McGraw Hill Book Company, 1969.

[2] W. Woo and D. V. Giri, "Directing HPM Radiation at Targets in Far Fields," HPM Research Note, Physics International Company, January 1988.

[3] C. E. Baum, "Focused Aperture Antennas," Sensor and Simulation Note 306, 19 May 1987.

[4] J. Benford, H. Sze, W. Woo, R. R. Smith and B. Harteneck, "Phase Locking of Relativistic Magnetrons," *Physical Review Letters*, Vol. 62, No. 8, 20 February 1989, pp. 969-971.

[5] Y. Rahmat-Samii, "Subreflector Extension for Improved Efficiencies in Cassegrain Antennas - GTD/PO Analysis," *IEEE Trans. on Antennas and Propagation*, Vol. AP-34, No. 10, October 1986, pp. 1266-1269.

[6] J. Ronen and R. H. Clarke, "Monitoring Techniques for Phased-Array Antennas," *IEEE Trans. on Antennas and Propagation*, Vol. AP-33, No. 12, December 1985, pp. 1313-1327.

[7] A. Papoulis, *Probability, Random Variables, and Stochastic Processes*, McGraw Hill, 1965.

[8] S. Ramo, J. R. Whinnery and T. Van Duzer, *Fields and Waves in Communication Electronics*, John Wiley, 2nd edition, 1984.

[9] *Reference Data for Radio Engineers*, Published by Howard W. Sams & Co., Sixth edition 1975, Section 25-8.

[10] C. E. Baum, "Some Features of Waveguide/Horn Design," Sensor and Simulation Note 314, 18 November 1988.

[11] R. Gomer, *Field Emission and Field Ionization*, Harvard University Press, Cambridge, Massachusetts, 1961.

[12] S. A. Schelkunoff and H. T. Friis, *Antennas-Theory and Practice*, Wiley, 1952, p. 526.

[13] E. H. Braun, "Gain of Electromagnetic Horns," *Proc. IRE*, Vol. 41, January 1953, pp. 109-115.

[14] E. H. Braun, "Some Data for the Design of Electromagnetic Horns," *IEEE Trans. on Antennas and Propagation*, Vol. AP-4, January 1956, pp. 29-31.

[15] A. W. Love, "The Diagonal Horn Antenna," Microwave Jornal, Vol V. March 1962, pp. 117-122.

[16] Special Issue (I) on High-Power Microwave Sources, *IEEE Trans. on Plasma Science*, December 1985.

[17] Special Issue (II) on High-Power Microwave Sources, *IEEE Trans. on Plasma Science*, April 1988.

[18] Special Issue (III) on High-Power Microwave Sources, *IEEE Trans. on Plasma*

Science, June 1990.

[19] H. K. Florig, "The Future Battlefield: a blast of gigawatts?" *IEEE Spectrum,* March 1988, pp. 50-54.

[20] J. Benford, "High-Power Microwave Simulation Development," *Microwave Journal*, December 1987.

[21] J. Swegle, "Pulsed Sources of High-Power Microwaves: The State of the Art," NEM-1990, University of New Mexico, Albuquerque, NM, May 21-24, 1990.

[22] *High-Power Microwave Sources*, Edited by V. L. Granatstein and I. Alexeff, ArTech House 1987.

[23] Y. Carmel, K. R. Chu, M. Read, A. K. Ganguly, D. Dialetes, R. Seeley, J. S. Levine, and V. L. Granatstein, *Physical Review Letters,* Vol. 50, 112, 1983.

[24] G. Bekefi and T. J. Orzechowski, *Physical Review Letters,* Vol. 37, (1976), 379.

[25] A. Palevsky, "Generation of Intense Microwave Radiation by the Relativistic e-Beam Magnetron(Experiment and Numerical Simulation)," Ph.D. Thesis, M.I.T., 1980.

[26] J. G. Wang, R. M. Gilgenback, J. J. Choi, C. A. Outten and T. A. Spenser, "Frequency-Tunable, High-Power Microwave Emission from Cyclotron Autoresonance Maser (CARM) Oscillation and Gyrotron Interactions," *IEEE Trans. on Plasma Science,* Vol. 17, No. 6, December 1989.

[27] G. A. Huttlin, M. S. Bushell, D. B. Conrad, D. P. Davis, K. L. Ebersole, D. C. Judy, P. A. Lezcano, M. S. Lits, N. R. Pereira, B. G. Ruth, D. M. Weidenheimer, and F. J. Agee, "The Reflex-Diode HPM Source on Aurora," Special Issue (III) on High-Power Microwave Sources, *IEEE Trans. on Plasma Sciences,* June 1990.

[28] J. Benford, H. Sze, W. Woo, R. R. Smith, and B. Harteneck, "Phase Locking of Relativistic Magnetrons," *Physical Review Letters*, Vol. 62, No. 8, 20 February 1989, pp. 969-971.

[29] C. E. Baum, " Combining RF Sources Using C_N Symmetry, " Circuit and Electromagnetic System Design Notes, Weapons Laboratory, 6 June 1989.